Progress toward divertor detachment on TCV within H-mode operating parameters

OPEN ACCESS
IOP Publishing
Plasma Physics and Controlled Fusion
Plasma Phys. Control. Fusion **61** (2019) 065024 (19pp)
https://doi.org/10.1088/1361-6587/ab140e

Progress toward divertor detachment on TCV within H-mode operating parameters

J R Harrison[1], C Theiler[2], O Février[2], H de Oliviera[2], R Maurizio[2], K Verhaegh[2,4], A Perek[4], A Karpushov[2], B Lipschultz[3], B P Duval[2], X Feng[6], S Henderson[1], B Labit[2], B Linehan[5], A Merle[2], H Reimerdes[2], U Sheikh[2], C K Tsui[2,7], W A J Vijvers[4], C Wüthrich[1], the TCV team[8] and the EUROfusion MST1 team[9]

[1] CCFE, Culham Science Centre, Abingdon, Oxon, OX14 3DB, United Kingdom
[2] Ecole Polytechnique Fédérale de Lausanne (EPFL), Swiss Plasma Center (SPC), Lausanne, Switzerland
[3] York Plasma Institute, Department of Physics, University of York, Heslington, York, YO10 5DD, United Kingdom
[4] DIFFER—Dutch Institute for Fundamental Energy Research, De Zaale 20, 5612 AJ Eindhoven, The Netherlands
[5] Plasma Science and Fusion Center MIT, Cambridge, MA 02139, United States of America
[6] Centre for Advanced Instrumentation, Durham University, South Road, Durham, DH1 3LE, United Kingdom
[7] University of California San Diego (UCSD), San Diego, CA, United States of America

E-mail: james.harrison@ukaea.uk

Received 28 September 2018, revised 14 March 2019
Accepted for publication 27 March 2019
Published 16 May 2019

Abstract

Recent experiments on Tokamak à Configuration Variable have made significant progress toward partial detachment of the outer divertor in neutral beam heated H-mode plasmas in conventional and alternative divertor configurations. The heating power required to enter H-mode was measured in a range of divertor configurations. It is found that at the core densities most favourable for H-mode access, the L–H threshold power is largely independent of the poloidal flux expansion and major radius of the outer divertor, and in the snowflake minus configuration. A factor 2 reduction in the outer divertor power load was achieved in ELM-free (using a fuelling and nitrogen seeding) and ELMy (using nitrogen seeding) H-mode plasmas. No significant reduction in the outer divertor particle flux was achieved in the ELM-free scenarios, compared with ~30% reduction in the most strongly detached ELMy cases. The poloidal flux expansion at the outer divertor was not found to significantly alter the cooling of the divertor in the ELM-free scenarios.

Keywords: plasma physics, tokamak, divertor, divertor detachment, TCV

(Some figures may appear in colour only in the online journal)

1. Introduction

The reliable operation of future high-power density magnetic confinement fusion reactors such as ITER [1] and DEMO [2, 3] requires that the power and particles leaving the confined plasma can be exhausted in such a way that avoids the limits of plasma-facing materials in the divertor and first wall. In ITER, this material limit for steady-state power loads is ~10 MW m^{-2} [4], and lower in DEMO [2]. For example, in a

[8] See the author list of S Coda *et al* 2017 *Nucl. Fusion* **57** 102011.
[9] See the author list of 'H Meyer *et al* 2017 *Nucl. Fusion* **57** 102014'.

DEMO reactor with a net electric power output of 500 MW [2], if the material limit is taken to be 5 MW m^{-2}, it is expected that >95% of the heating power will need to be exhausted via radiation.

Several potential solutions are currently being explored to address this challenge. They include introducing impurities into the confined plasma to exhaust a significant fraction of the heating power as radiation and alternatives to the conventional divertor configuration, such as the X-divertor [5, 6], snowflake [7], Super-X [8], X-point target [9] and the flux-tube-expansion divertor [10]. These aim to reduce the concentration of power and particle loads to the divertor through a combination of geometry, promoting access to detachment [11–13] and enhancing transport across the magnetic field [14–18].

Previous studies of divertor detachment on Tokamak à Configuration Variable (TCV) have predominantly been carried out in L-mode plasmas, including a detailed characterisation of detachment in single null configurations [19–22] (including the X-divertor in [19, 23]), snowflake [15, 24, 25], and other alternative geometries [23] including variants of the Super-X and X-point target configurations. The following contribution builds on this work to explore routes toward detachment in high (pedestal) pressure ELM-free and ELMy H-mode plasmas heated with neutral beam injection. ELM-free plasmas are diagnosed in greater detail with diagnostics that can capture the rapid evolution of these shots, but are currently unable to resolve the inter-ELM conditions with the same fidelity. A combination of deuterium fuelling and nitrogen seeding from the divertor is used to promote cooling of the outer divertor leg and the onset of detachment.

The structure of this paper is as follows: in section 2 an overview of the experiments and key diagnostics pertinent to this study is presented. In section 3 the operational space in H-mode is characterised, including an experimental assessment of the power required to trigger an L–H transition in different divertor configurations, the pedestal properties and their relationship with the triggering of ELMs, and the limits to H-mode operation. In section 4, an overview of detachment studies in ELM-free plasmas is presented, including a comparison of using deuterium fuelling and seeding to cool the outer divertor on the core, pedestal and divertor, and the effects of varying the poloidal flux expansion at the outer divertor. In section 5, an overview of ELMy H-mode experiments is presented, where nitrogen seeding is used to promote detachment, with a similar structure to the analysis applied to the ELM-free experiments. In section 6, key observations from these experiments are summarised, similarities and differences identified between observations of detachment in ELM-free, ELMy H-mode and L-mode plasmas and a motivation for future experiments is given.

2. Overview of experiments and key diagnostics

The TCV tokamak [26–28] at EPFL is a conventional aspect ratio device (R/a is typically $0.88/0.25 \sim 3.5$, where R and a are major and minor radii respectively) with toroidal field $B_t \sim 1.44$ T and extremely high flexibility to vary the plasma shape, afforded by 16 independently controlled poloidal field coils and an open vessel structure. Recent improvements to TCV include a Neutral Beam Injector (NBI) that can inject up to 1 MW of power at 25 keV [26, 29] used extensively in this study.

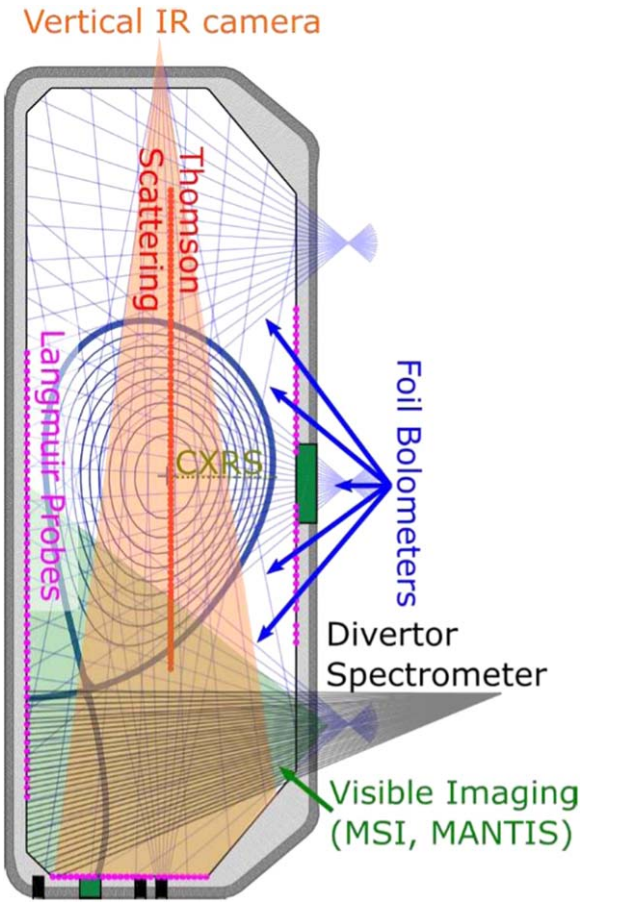

Figure 1. Overview of the main core and divertor diagnostics used in this study.

TCV contains an extensive array of divertor diagnostics, summarised in figure 1 including 114 Langmuir probes (LPs) mounted in the inner and outer walls and the floor of the divertor [30, 31]. The probe bias voltage is normally swept with a frequency of 330 Hz from −120 to +80 V. The inner and outer strike points are monitored with two infra-red (IR) cameras [17] with a frame rate up to 25 kHz. Estimates of radiative losses and their distribution are provided by 8 gold foil pinhole cameras with 8 channels per camera [32]. Tomographic reconstructions of the bolometer data are routinely performed to estimate the radiation emissivity across the device. Over the course of this study, 2 filtered camera diagnostics, multi-spectral imaging (MSI) [33] and Multi-spectral Advanced Narrowband Tokamak Imaging System (MANTIS) [34] have been in use. They normally view the lower divertor to monitor the spatial distribution of spectral emission lines in the visible spectrum, from the deuterium Balmer series and low charge states of carbon, helium and nitrogen. The data presented here include tomographic

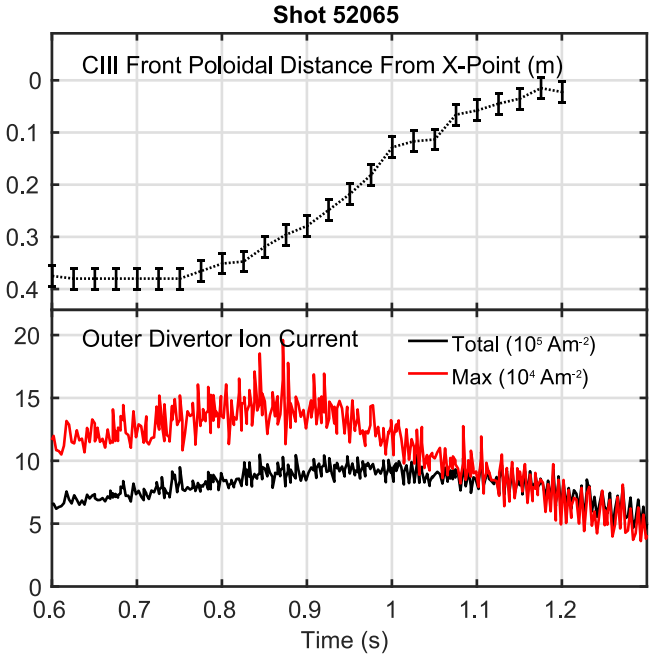

Figure 2. Time evolution of the CIII emission front location along the outer leg (top) and the total and peak ion current to the outer divertor (bottom) during an L-mode ohmically heated density ramp experiment [21]. A reduction in the ion current, characteristic of the onset of detachment, occurs when the front is approximately half way between the target and the X-point.

reconstructions of spectrally uncalibrated spectral line emissivities of impurity line emission (filtered for a CIII multiplet at 464.74, 465.03, 465.14 nm with a contribution from a NII 463.31 nm line) and deuterium Balmer lines on an axisymmetric unstructured triangular mesh with a typical cell size of ~5 mm that conforms with the poloidal cross-section of the TCV inner wall. Inverted line emission profiles have been used extensively in the community to characterise the divertor volume, e.g. on DIII-D [35], C-Mod [36], JET [37], ASDEX Upgrade [38] and similar tomographic inversion techniques are applied here. In this study, the movement of CIII emission toward the X-point and the brightness of deuterium Balmer emission are used to assess the progress toward detachment and to indicate the role of ionisation sources and recombination sinks in mitigating the divertor particle flux. For example, figure 2 shows the movement of the CIII emission 'front' from the target, characterised by the poloidal distance along the outer leg from the X-point where the emission drops to 50% of its peak value.

Nitrogen seeding is used extensively in the experiments presented here, unlike previously reported studies where deuterium fuelling is used to approach detachment [19, 21, 23, 39]. As indicated in the previous paragraph, the interpretation of the CIII filtered camera data is complicated by a contribution from a NII line within the filter bandpass, which will elevate the measured signal and could affect the spatial distribution of the emission. The effect of this additional impurity contribution on the position of the emission front was estimated by comparing with measurements from a multi-chord Divertor Spectroscopy System (DSS) [22] to independently measure the spectral emission within the bandpass of the filter. This allows for comparison with intensity profiles of individual CIII and NII emission lines estimated with the spectrometer, and to estimate the position of the different emission fronts. This comparison is shown in figure 3, where it is found that there is generally good agreement between the measured emission profiles from the camera and spectrometer data within the bandpass of the camera filter and with the CIII emission profile. The front positions estimated from the DSS data with the camera filter applied and from CIII emission are separated by a poloidal distance of 1 cm. This suggests that NII emission does not significantly affect the inferred CIII emission front location. However, under certain conditions not shown here, such as experiments with higher nitrogen seeding rates, the NII contamination can be greater, leading to <2 cm shift in the front position. The uncertainty in the front position derived from the camera data, due to inaccuracies in the spatial calibration and imperfections in the tomographic reconstruction are conservatively estimated to be ~1 cm. Consequently, the uncertainty in the estimated impurity front location reported here is estimated to be ± 2 cm (compared with a typical poloidal divertor leg length of ~35 cm).

Routine measurements of the upstream electron temperature and density profiles are provided by a Thomson scattering system [40] containing 3 20 Hz Nd:YAG lasers and a vertical spatial resolution that varies from 12 mm to measure the steep pedestal profiles to 36 mm in locations typically monitoring the confined plasma. Radial profiles of the ion temperature profiles in the core are provided by a Charge-Exchange Recombination Spectroscopy system.

These experiments studied variants of the single null divertor configuration in an ELM-free H-mode scenario with a plasma current, I_p of 340 kA (edge safety factor $q_{95} \sim 2.4$, minor radius a ~0.21, elongation $\kappa \sim 1.61$) and 200 kW of NBI heating and an ELMy H-modes with $I_p = 210$ kA ($q_{95} \sim 3.8$, $a \sim 0.22$, $\kappa \sim 1.63$), 170 kA ($q_{95} \sim 4.6$, $a \sim 0.23$, $\kappa \sim 1.49$) and 140 kA ($q_{95} \sim 3.9$, $a \sim 0.21$, $\kappa \sim 1.51$) and 1 MW of NBI heating. In all cases, the ion ∇B drift is directed downward toward the primary X-point, as this is favourable for H-mode access. This differs from the majority of previously reported L-mode detachment experiments [19, 21–23] and is expected to alter the onset and evolution of detachment via changes in transport due to cross-field drifts [41, 42] and other effects. Unless otherwise stated, gas puffing into the divertor from valves situated near the floor of TCV consisted of deuterium fuelling directed toward the Scrape-Off Layer (SOL) of the outer leg and nitrogen seeding into the private flux region.

3. H-mode operating space

This section summarises findings from experiments to estimate the power crossing the separatrix required to trigger an L–H transition and its variation with divertor configuration, the limits to H-mode operation and the parameter space where operation in ELM-free and ELMy H-mode regimes is

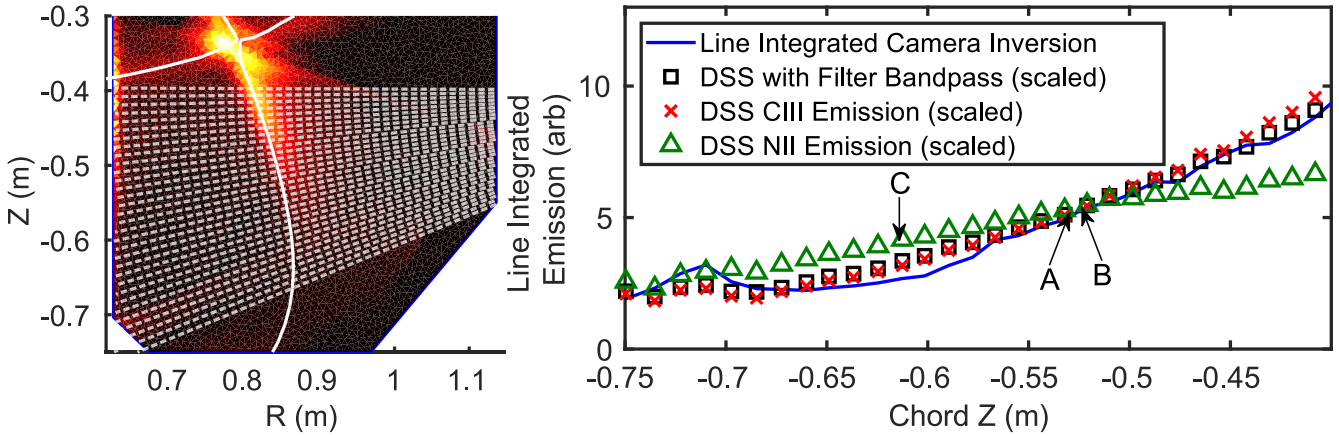

Figure 3. (Left) Inverted camera data filtered primarily for CIII emission with the DSS spectrometer viewing chords overlaid. (Right) Profiles of the emissivity shown on the left integrated along the DSS chords, the DSS emission within the CIII filter bandpass, and purely CIII and NII emission. The various front locations derived from these emission profiles, taken to be when the emission drops to 50% of the peak value above the baseline at $Z = -0.75$ m, are indicated by A, B, C from the DSS data with the filter bandpass applied, CIII and NII emission lines respectively.

possible. This information is summarised in a schematic representation of the operating space of the scenarios studied in terms of quantities most relevant to divertor physics studies, including the parallel heat flux, radiated power fraction and the upstream separatrix electron density, which effectively act to constrain the level of detachment that can be achieved whilst operating in H-mode.

3.1. Access to H-mode

Operation in H-mode requires the power crossing the separatrix to reach (or exceed) a threshold value in order to trigger the transition from L-mode. The threshold is known to depend on several parameters, including but not limited to the core density, X-point height and divertor geometry, and has been studied extensively on several devices including JET [43], NSTX [44], DIII-D [45], ASDEX Upgrade [46], EAST [47], C-Mod [48], MAST [49], TCV [50] and others. In the current experiments at TCV, the threshold power was estimated by ramping the NBI power from 0.1 to 1 MW over 700 ms, slow enough that effects due to the finite energy confinement time (∼ms) and fast ion slowing down time (∼10 ms [51]) can be neglected in the forthcoming analysis. The total plasma heating power is calculated from a sum of the ohmic heating (due to the plasma current and finite plasma resistivity) and the NBI power absorbed by the plasma, estimated from ASTRA [52, 53] simulations using measured plasma profiles as input. Using this approach, the power required to trigger an L–H transition was estimated in 210 kA single null plasmas where the poloidal flux expansion from the outer mid-plane to the outer divertor, henceforth referred to as $f_{x,\mathrm{OSP}}$ (a more detailed description is given in [23]), was varied from 4 to ∼8.5 and the major radius of the strike point was 0.75 m. Threshold measurements were also made in configurations where the outer strike point major radius, henceforth referred to as R_T, was increased to ∼1.06 m (with $f_{x,\mathrm{OSP}} \sim 2.3$) and in the snowflake minus configuration.

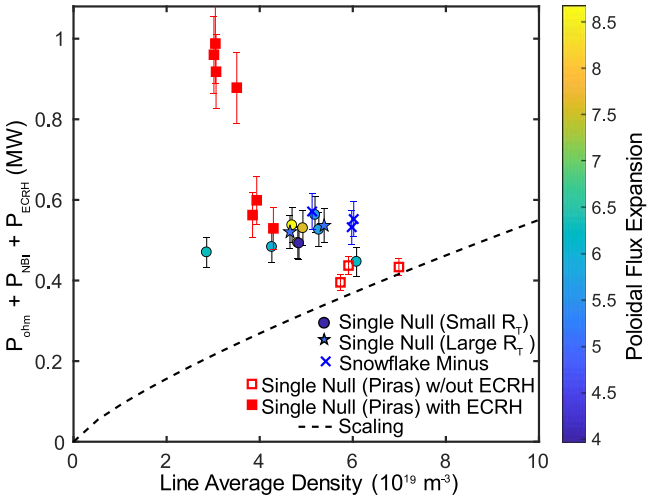

Figure 4. Heating power applied at the L–H transition as a function of core line average density single null divertor configurations of different outer target poloidal flux expansion and major radius and snowflake configurations with NBI heating. Comparison is made with previously published data from single null ECRH and ohmic heated discharges [55] and the widely used scaling by Martin (dashed curve) [54].

The results from this study are summarised in figure 4, showing the variation in the L–H threshold power P_thr with the line average density n_e for the divertor configurations outlined. A scaling of $P_\mathrm{thr}(\mathrm{MW}) = 0.049\overline{n_e}(10^{20}\ \mathrm{m}^{-3})^{0.72}B_t(\mathrm{T})^{0.8}S(\mathrm{m}^2)^{0.94}$ where S is the surface area of the confined plasma is typically ∼10 m^2 in these shots and $\overline{n_e}$ is the line average density measured using interferometry. Comparison is made with previous measurements in ohmic and ECRH heated plasmas [55] over a wider density range, which suggests the data collected in this study are close to the density at which the threshold power is at a minimum. However, more data is needed to ascertain whether the density required to minimise the L–H threshold varies significantly with the divertor configuration. The data from the single null configuration with $f_{x,\mathrm{OSP}} \sim 6.5$ (indicated by light

green circles in figure 4) exhibit a weaker variation with density compared with the data obtained using ECRH heating, which could be due to the difference in heating technique. Furthermore, L–H threshold estimates in these divertor configurations over the range of line average density spanning 5–6 $\times$ 10^{19} m^{-3} suggest that divertor geometry does not significantly influence the threshold power. However, there is currently insufficient data to ascertain whether the divertor configuration affects the threshold power over a wider range of operating conditions.

3.2. Limits to ELMy H-mode operation

In order to achieve quasi-stationary conditions in H-mode, a regularly ELMing regime is required or ELM suppressed or naturally ELM-free regimes with enough transport from the edge into the SOL to regulate the density. In the ELM-free case studied here, the line average density continually rises through the H-mode phase at a rate of $\sim$7 $\times$ 10^{20} m^{-3} s^{-1} until a disruptive limit is reached, which is described in more detail in the next section. Therefore, in the absence of a stationary ELM-free scenario, it is desirable to achieve and maintain a steady ELMing regime in attached and detached divertor conditions.

In the ELMy H-mode plasmas studied here, excessive deuterium gas fuelling can result in a transition to an ELM-free regime (leading to a loss of quasi-stationarity) or a back-transition to L-mode. To quantify the domain of ELMy and ELM-free regimes, in terms of the pedestal top temperature and density T_e^{ped} and n_e^{ped} respectively, a database was compiled of Thomson scattering measurements of pedestal temperature and density profiles in both ELMy (from 10% to 90% of the ELM cycle, to include the pedestal profile evolution between ELMs) and ELM-free regimes. Estimates of the pedestal height and width were obtained by fitting mtanh functions [56] to these profiles. The resulting database is shown in figure 5 (upper plot), showing a clear delineation between the ELMy regime where $n_e^{ped} \leqslant 5 \times 10^{19}$ m^{-3} and a transition to an ELM-free regime at higher densities. No such threshold is apparent in terms of T_e^{ped}. This threshold is further illustrated in figure 5 (lower plot), where a high current ELMing plasma ($I_p = 390$ kA, $q_{95} = 2.10$) is fuelled in order raise the pedestal density, which causes a transition to ELM-free when the pedestal top density exceeds 5 $\times$ 10^{19} m^{-3}. It is not clear whether the pedestal top density or another correlated quantity, such as the separatrix density, is responsible for setting this limit. This threshold imposes a constraint on the highest achievable density at the separatrix in ELMy H-modes. If it is assumed that the separatrix density is at most 50% of n_e^{ped}, this suggests it cannot exceed $\sim$2.5 $\times$ 10^{19} m^{-3} unless this constraint is relaxed, e.g. by modifying the plasma shaping or increasing the heating power to promote the triggering of ELMs. Higher density at the pedestal top can be achieved in ELM-free H-modes, thereby improving access to detachment, albeit temporarily before the core density ramps to an operating limit.

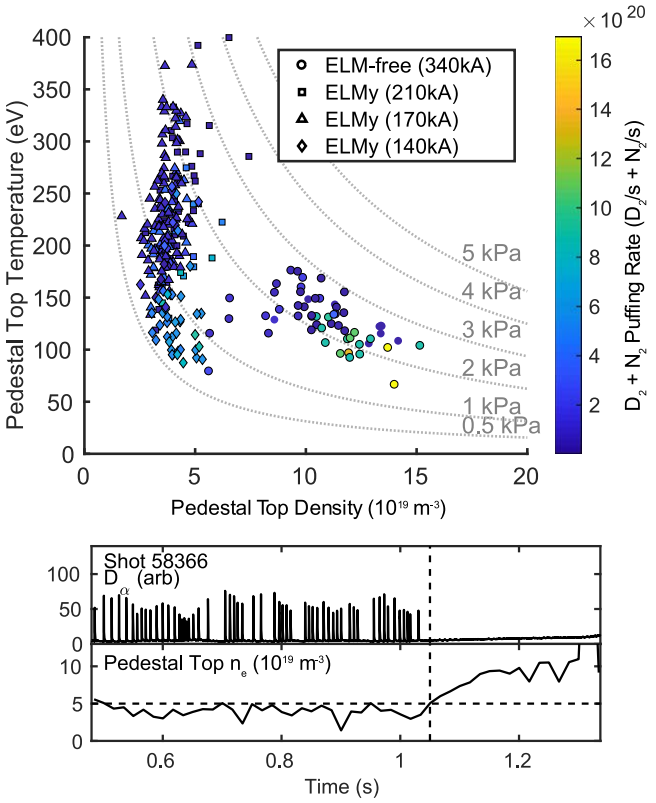

Figure 5. Upper—electron density and temperature at the pedestal top in ELM-free and ELMy H-mode scenarios. Lower—Transition from ELMy to ELM-free regime in a shot when the pedestal top density exceeds 5 $\times$ 10^{19} m^{-3}.

3.3. H-mode operating limits

The ELM-free plasmas studied here are characterised by a steady rise of the core line average density until a disruption occurred, typically due to a loss of control of the vertical position of the plasma. In the absence of fuelling and seeding from the divertor, disruptions typically occur when the core line average density reaches $\sim$80% of the Greenwald density limit [57] (calculated as an average over 4 shots with a 3% standard deviation), defined as $n_G(10^{20}\ m^{-3}) = \frac{I_p(MA)}{\pi a^2(m^2)}$ where I_p is the plasma current and a is the minor radius of the core plasma. The fraction of the Greenwald limit is given as $\frac{\overline{n_e}}{n_G}$, where $\overline{n_e}$ is defined previously. The addition of deuterium fuelling and nitrogen seeding alone reduced this disruptive limit to $\sim$76% and $\sim$70% respectively (averaged over 9 shots and 3 shots with 3% and 7% standard deviation respectively), and a combination of fuelling and seeding did not lower the limit significantly compared with measurement uncertainties, to $\sim$69% (averaged over 2 shots with 4% standard deviation).

In the ELMy H-mode regime, the principal limits are set by the power required to stay in H-mode and the transition to an ELM-free regime. Strong nitrogen seeding leads to a steady reduction of the ELM amplitude and eventually a transition back to L-mode. This behaviour is observed in these experiments when the proportion of the power crossing the separatrix, P_{SOL} that is radiated in the SOL and divertor

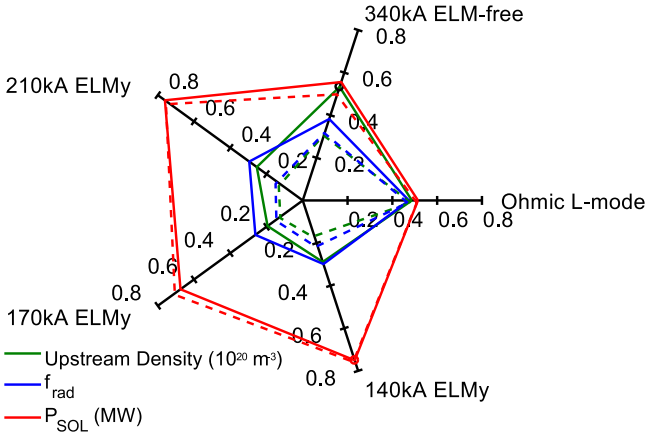

Figure 6. Comparison of the H-mode experiments, in terms of the upstream density (black), $f_{\rm rad}$ (blue) and power crossing the separatrix, $P_{\rm SOL}$ (red), in the ELMy and ELM-free scenarios studied, in the presence (solid) and absence (dashed) of additional fuelling and seeding to promote divertor detachment. For comparison, these quantities are plotted for the ohmic L-mode shot 52 065 at the detachment threshold [21, 22].

(i.e. $P_{\rm rad}^{\rm div\text{-}SOL}/P_{\rm SOL} = f_{\rm rad,SOL}$) is ~20%–30% (as shown in figure 21).

3.4. Overview of the H-mode operating space

Taking the considerations mentioned in the preceding sections into account, the H-mode operating scenarios for these experiments, in terms of quantities relevant for studies of divertor detachment, is shown in figure 6. The upstream density is estimated from performing mtanh fits to the pedestal temperature and density profiles measured from 70% to 99% of the ELM cycle, and enforcing the constraint that the separatrix temperature agree with estimates from the two-point model [58], which requires the upstream parallel heat flux ($q_{||}$), upstream separatrix density and the radial width of the SOL $\lambda_{\rm q}$, as inputs. The parallel heat flux is estimated from the expression [59]:

$$q_{||} = \frac{B_{{\rm tot},u}}{B_{p,u}} \frac{c_{\rm div} P_{\rm SOL}}{2\pi R_u \lambda_q},$$

where $B_{{\rm tot},u}$ and $B_{p,u}$ are the total and poloidal magnetic field components at the outer mid-plane at major radius R_u, $c_{\rm div}$ is the proportion of the power crossing the separatrix that is flowing to the divertor leg studied, $P_{\rm SOL}$ is the power crossing the separatrix and λ_q is the width of the SOL at the outer mid-plane. λ_q is estimated from the expression:

$$\lambda_q({\rm mm}) = 9.0\left(\frac{340}{I_p({\rm kA})}\right)$$

derived from IR thermography measurements of radial heat flux profiles in the attached phase of ELM-free H-mode shots and comparison with LP data, and the observation in [60] that $\lambda_{\rm q}$ scales approximately with I_p^{-1}. $P_{\rm SOL}$ is calculated from considerations of the global power balance, discussed in the following sections. In ELMy scenarios, the inter-ELM power balance is estimated using foil bolometer measurements of the

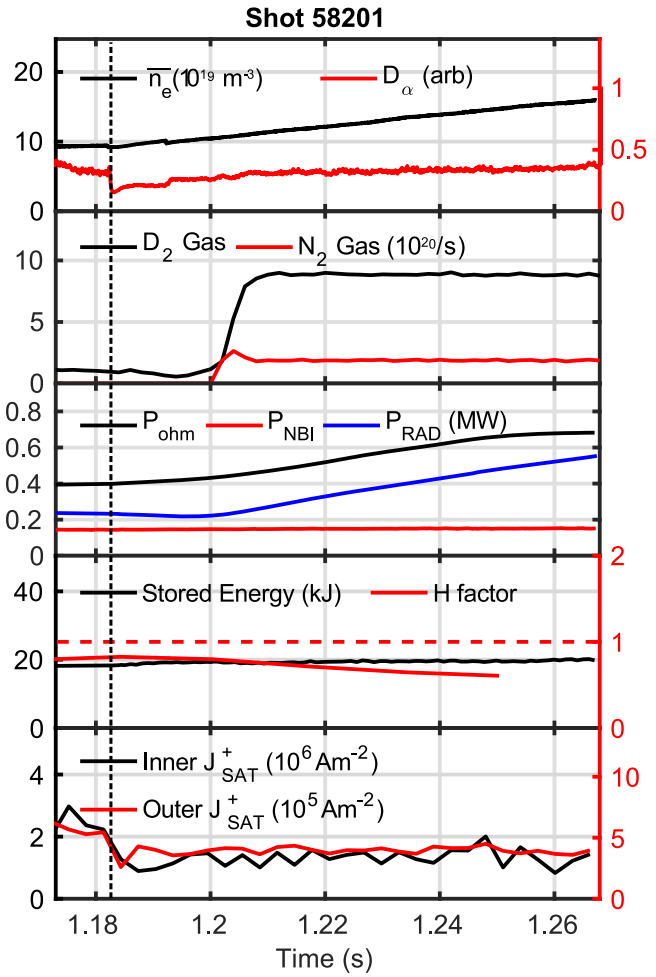

Figure 7. Overview of a typical ELM-free H-mode shot, showing the evolution of the line average density, divertor D_α emission, gas fuelling and seeding rates, plasma power sources and sinks, stored energy and confinement quality and the total particle flux to the inner and outer divertors. The L–H transition is indicated by the dashed vertical line.

radiation between ELMs and the average energy loss due to ELMs estimated by the change in diamagnetic flux.

This exercise allows operating conditions in the absence and presence of additional gas fuelling and seeding to promote detachment to be compared between the H-mode scenarios explored and with the detachment threshold observed in 340 kA ohmic L-mode plasmas studied previously [21, 22]. It is found that the application of additional fuelling and seeding does not significantly influence the parallel heat flux, but can increase both $f_{\rm rad}$ (the ratio of the total radiated power and heating power) and the upstream density by a factor ~2 (see figure 7).

Access to detachment in a given scenario can be estimated by considering the target electron temperature $T_{\rm t}$ predicted by the modified two-point model [62]:

$$T_t = \frac{q_{||}^2}{n_u^2}\left(\frac{2\kappa_{0e}}{7q_{||}L_{||}}\right)^{4/7} \frac{2\,m_i}{\gamma^2 e^2} \frac{(1-f_{\rm pow})^2}{(1-f_{\rm mom})^2(1-f_{\rm conv})^{4/7}},$$

where $L_{||}$ is the parallel connection length from the outer mid-plane to the outer divertor, κ_{0e} is the electron heat

conductivity, m_i is the ion mass, γ is the sheath heat transmission coefficient, e is the elementary charge, f_{pow} and f_{mom} represents the fraction of the upstream heat flux and total plasma pressure dissipated in the SOL and divertor respectively and f_{conv} represents the fraction of $q_{||}$ carried by convection. All other terms have been defined previously. The model suggests the conditions most favourable for detachment, through reducing T_t include high upstream density, operating at the minimum $q||$ required to achieve good core confinement, increasing $L_{||}$ and maximising dissipation of power and pressure in the SOL and divertor. On this basis, ELM-free H-modes offer some advantages in terms of operating at higher upstream density and low P_{SOL}, although not necessarily at significantly reduced upstream heat flux due to the narrower width of the SOL, λ_q.

4. ELM-free H-mode experiments

4.1. General observations

As outlined in figure 6 and previous sections, ELM-free H-mode scenarios are characterised by relatively high pedestal top density, $n_e^{ped} > 5 \times 10^{19}\,m^{-3}$, moderate pedestal top temperature $100\,eV < T_e^{ped} < 180\,eV$ and moderate parallel heat flux $\sim 20\,MW\,m^{-2}$ (estimated assuming $\lambda_q = 9\,mm$, as discussed in the previous section) compared with the ELMy H-mode scenarios discussed in the next section. This means these scenarios are amenable to approaching the conditions required for divertor detachment. An overview of a typical ELM-free H-mode plasma with fuelling and nitrogen seeding from the lower divertor is shown in figure 7, showing a strong increase in the line average density from $\sim 1.0 \times 10^{20}\,m^{-3}$ up to $1.6 \times 10^{20}\,m^{-3}$ and a corresponding increase in both the ohmic heating power, due to the higher electrical resistivity of the core plasma at fixed plasma current, and total radiated power. The plasma stored energy increases by ~10%, heating power increases by ~50%, leading to the energy confinement time, τ_E, (calculated from the ratio of the plasma stored energy and the total heating power minus the rate of change of stored energy) decreasing by ~40%. These factors, together with the ~70% increase in line average density, lead to the H factor (the energy confinement time normalised to the predicted value based on the IPB98(y, 2) scaling [61]) reducing from ~0.8 to ~0.6. These figures are typical for this scenario, based on an analysis of 15 otherwise similar shots with different fuelling and seeding rates. The total particle flux to the inner and outer divertors is approximately constant throughout the H-mode phase unless stronger fuelling and seeding are applied.

4.2. Effects of fuelling and seeding

4.2.1. Global power balance. In order to quantify the progress toward reaching divertor detachment, it is instructive to start from the consideration of the main sources and sinks of power to and from the SOL respectively. The main sources of power to the plasma are from ohmic (resistive) heating P_{ohm} and NBI P_{NBI}^{inj}. Estimates of the ohmic heating power are derived from

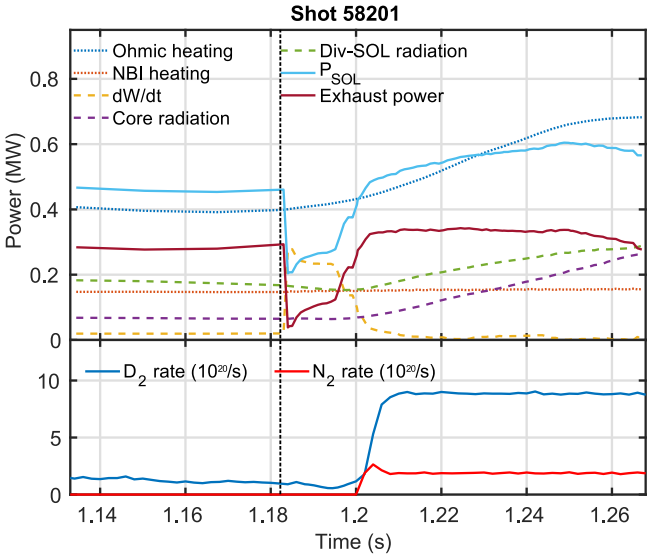

Figure 8. Global power balance in a nitrogen seeded ELM-free shot. In the upper plot, the power sources are indicated as dotted lines and sinks as dashed lines. The power crossing the separtrix, P_{SOL}, and the exhaust power (i.e. P_{SOL}-power radiated in the SOL and divertor) are plotted in solid lines. The gas fuelling and seeding rates are shown in the lower plot. The L–H transition is indicated by the dashed vertical line.

LIUQE [63] equilibrium reconstructions. The proportion of the injected NBI power absorbed by the plasma is estimated from a database of ASTRA simulations of 16 shots from these experiments to estimate a scaling of the fraction of the neutral beam power P_{NBI}^{inj} delivered by the ion source absorbed by the plasma, f_{abs}. These simulations account for losses due to charge-exchange and orbit losses. The absorbed power is found to vary most strongly with line average density, $\overline{n_e}$, according to the relationship $f_{abs} = 0.73 - e^{-0.5\times10^{-19}\overline{n_e}(m^{-3})}$, which is to be expected given that the peaking of the temperature and density profiles is similar in these and the core plasma position and shape do not vary considerably. The primary power sinks are due to radiation, both inside and outside the core (P_{rad}^{core} and $P_{rad}^{div-SOL}$), and the rate of change of stored energy $\frac{dW}{dt}$, which plays a significant role immediately following the L–H transition. To quantify the progress toward detachment, the power crossing the separatrix is estimated by $P_{SOL} = P_{ohm} + f_{abs}P_{NBI}^{inj} - \frac{dW}{dt} - P_{rad}^{core}$. This power must be exhausted in the divertor and SOL or convected by the plasma to plasma-facing surfaces. By extension, the power deposited from the plasma to the divertor surfaces is expressed as the exhaust power, $P_{SOL} - P_{rad}^{div-SOL}$.

An overview of the power balance of a typical fuelled and nitrogen seeded ELM-free shot is shown in figure 8 (the time evolution of the main plasma parameters is shown in figure 7) to illustrate the time evolution of the power sources and sinks. In the 1–2 ms following the L–H transition, the plasma stored energy increases rapidly, resulting the dW/dt term having a strong impact on the overall power balance. Following this phase, the sources of power rise throughout the ELM-free phase due to an increase in the ohmic heating power. This rise

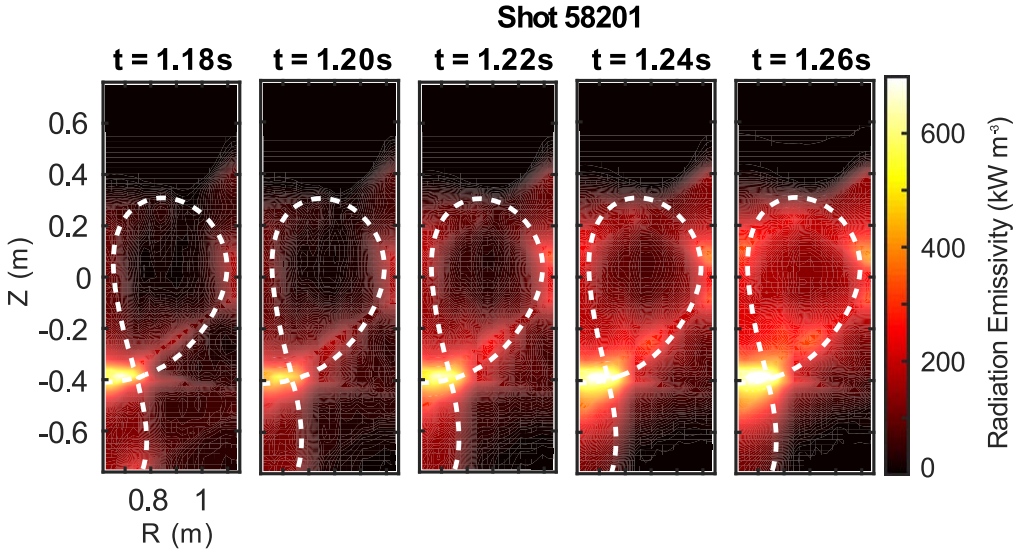

Figure 9. Radiation emissivity profiles estimated from tomographically inverted foil bolometer data taken from a nitrogen seeded ELM-free H-mode shot from the time following the L–H transition to just prior to a disruption.

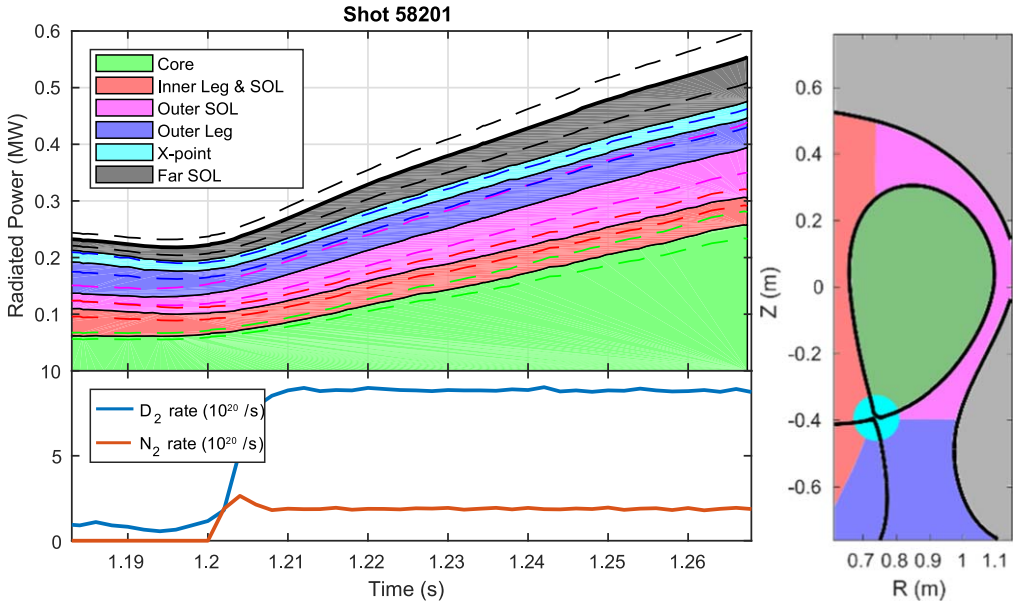

Figure 10. (Left) Breakdown of the radiated power measured by the foil bolometers in terms of its origin within the plasma for a nitrogen seeded ELM-free H-mode shot. The dashed lines indicate uncertainties in each measurement, estimated by varying the regularisation parameter used in the tomographic reconstructions. (Right) description of the plasma regions used in the left plot.

is compensated by an increase in the radiation both inside and outside the core that cause the exhaust power to roll over toward the end of the H-mode phase.

The evolution of the radiation losses and their distribution has been studied in detail by analysing the tomographically inverted foil bolometer data. In all ELM-free shots studied, the majority of the increase in radiation originates from the confined plasma, irrespective of the level of fuelling or seeding applied. In shot 58 201 the effective charge of the core plasma, estimated from soft x-ray measurements, increases strongly during the H-mode phase from ∼1.15 to 1.45. This suggests the increased core radiation is due to the higher impurity content in the core and higher electron density. However, the total radiation outside the confined plasma steadily increases with time due to emission from the SOL in the vicinity of the outer mid-plane and the far SOL, which could be due to sputtering of impurities from plasma-surface interactions or artefacts in the tomographic reconstructions.

As the divertor cools due to the injection of deuterium and nitrogen, the radiation from the outer leg recedes from the strike point toward the X-point and a commensurate increase in the radiation emissivity along the outer leg in the vicinity of the X-point, as shown in figure 9. A quantification of the power radiated from the different regions of the plasma is shown in figure 10 for the nitrogen seeded shot discussed in figures 8 and 9, confirming that the radiation from the core

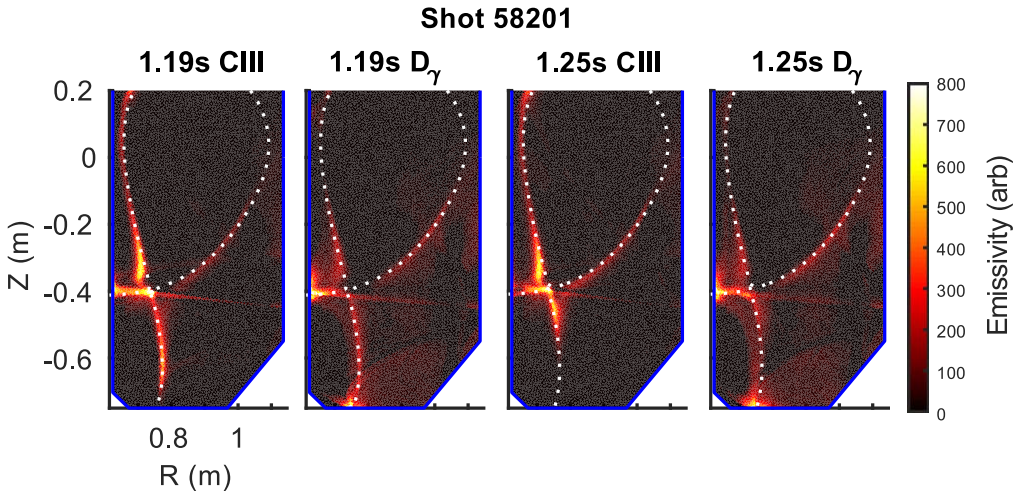

Figure 11. Inverted 2D emissivity profiles of impurity emission (labelled CIII) and deuterium Balmer γ emission at the start (a), (b) and end (c), (d) of the ELM-free H-mode phase with impurity seeding to promote cooling in the divertor.

increases most quickly, from ~30% of the total radiated power at the start of the H-mode phase to ~50% just prior to a disruption. The total power radiated in the inner and outer divertors is approximately constant throughout the density ramp, while the radiation at the X-point increases by 50% (although its contribution to the total radiated power is less than 8% throughout the H-mode phase). The inverted bolometer data suggest that this is due to radiation emissivity increasing, mitigating the decrease in the radiating volume as the front moves toward the X-point.

Inverted impurity emission and deuterium Balmer γ emission profiles from the MSI imaging diagnostic at the start and end of the fuelling and seeding phase is shown in figure 11. At the start of the fuelling and seeding phase, the impurity emission extends along the outer leg from the X-point to the vicinity of the strike point, then recedes toward the X-point prior to a disruption. The movement of the impurity emission toward the X-point is indicative of the radiation front receding in a similar manner, as previous L-mode experiments [23] found the two to be in reasonable agreement. The distribution of the deuterium Balmer γ emission is broadly unchanged, unlike previous L-mode experiments where a clear broadening of the emission near the target is observed [21]. At the highest seeding rates studied, e.g. shot 58 200 with a N_2 rate twice that of 58 201, the $D\gamma$ emissivity at the outer strike point reduces at the end of the seeding phase. This reduction in the Balmer line emission is instructive because if the population of the deuterium atomic states is dominated by electron impact excitation (as opposed to volume recombination), the line brightness is proportional to the ionisation source, which in turn governs the total particle flux to the divertor. DSS measurements of the ratio of the brightness of D_ε (396.9 nm) $/D_\delta$ (410.1 nm) emission lines suggest that excitation is the dominant source of emission. This highest value of this ratio (higher ratios indicate a stronger contribution from recombination) is ~0.35, compared with >0.5 measured in more deeply detached L-mode shots where recombination dominates [22].

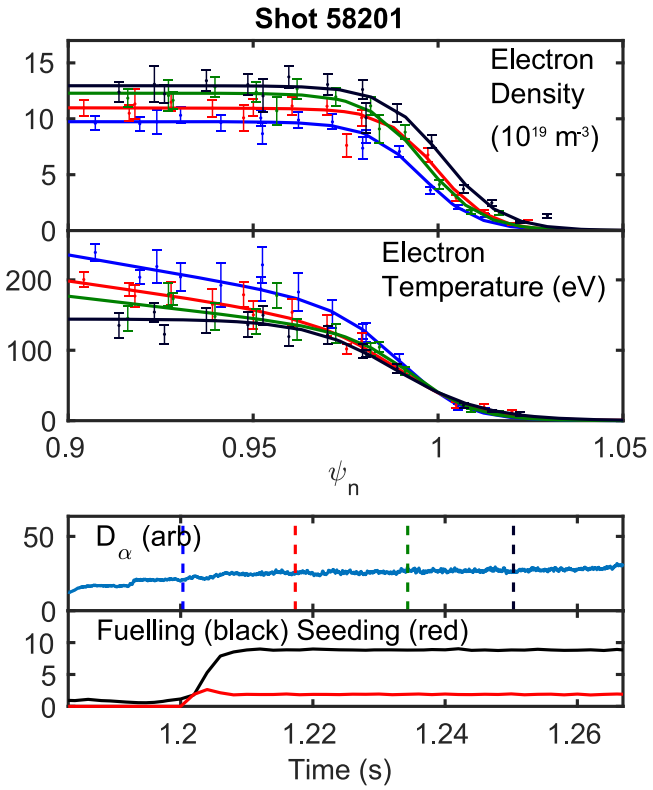

Figure 12. Fitted Thomson scattering profiles during the fuelling and nitrogen seeding phase of an ELM-free H-mode shot.

4.2.2. Pedestal profile evolution. The evolution of these ELM-free H-mode shots is rapid, typically lasting for less than 200 ms and is characterised by a rapid increase in the line average density. During the H-mode phase, the electron temperature and density profiles also changes substantially. A typical example of the evolution of the pedestal profiles is shown in figure 12, where mtanh fits to the Thomson scattering data during the fuelling and seeding phase are presented, using the two-point model to constrain the separatrix electron temperature as described in section 3.4. The pedestal top electron density is

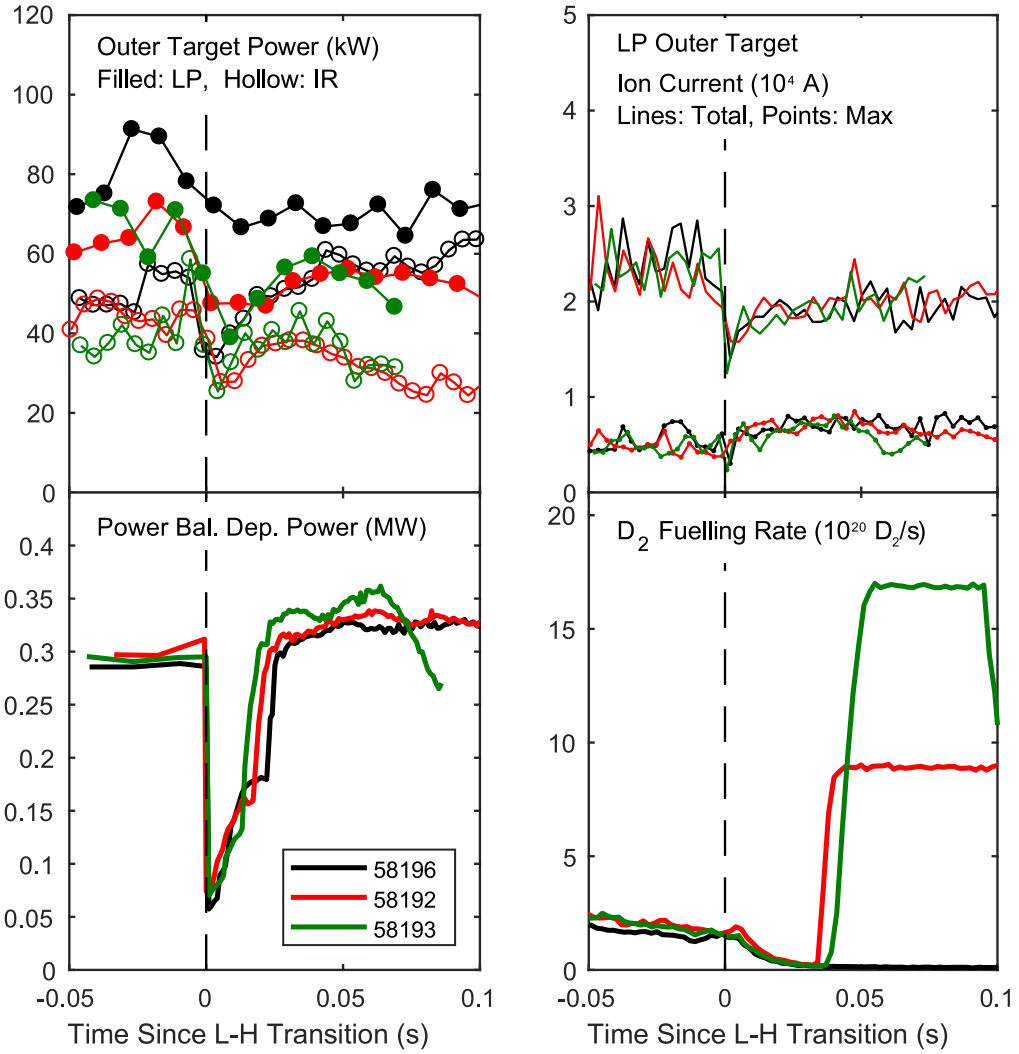

Figure 13. Evolution of the outer divertor power and particle loads in shots with varying fuelling from the lower divertor, from no fuelling (black), an intermediate fuelling rate (red) and highest rate (green). (Upper left) Total power incident to the outer divertor estimated with Langmuir probes (filled points) and IR thermography (hollow points), (upper right) total and maximum ion current to the outer divertor, (lower left) power incident to the outer divertor estimated from power balance, (lower right) divertor fuelling rate.

found to increase by ∼30% and the separatrix density to increase by a factor of ∼2. This behaviour is found to be independent of the level of fuelling or seeding. Conversely, the electron temperature at the pedestal top decreases by ∼15% and the separatrix temperature is approximately constant, as the variations in P_{SOL} are sufficiently small that they do not significantly modify the separatrix temperature. The gradient in the edge electron temperature profile is also observed to decrease over time, concomitant with a 20% reduction in the temperature close to the magnetic axis, from ∼500 eV at the start of the H-mode phase to ∼400 eV, accompanied by a commensurate increase in density.

4.2.3. Outer divertor power and particle loads. The influence of deuterium fuelling on the power and particle loads to the outer divertor were studied by running similar discharges with different levels of fuelling into the SOL region on the floor. The results of this scan are shown in figure 13, which shows the total power loads to the outer divertor, estimated using IR thermography and LP arrays, and total particle loads estimated by the probes. The power deposited to the divertor q_{dep} is estimated from the LP data using the relationship $q_{\mathrm{dep}} = en_e^t c_s^t(\gamma T_e^t + E_{\mathrm{pot}})$ where c_s is the ion acoustic velocity, given by $\sqrt{(T_e^t + T_i^t)/m_i}$ where the ion and electron temperatures are assumed equal, E_{pot} is the potential energy of each ion, the sum of the hydrogen ionisation energy (13.6 eV) and half of the Franck–Condon molecular dissociation energy (2.2 eV), γ is the sheath heat transmission factor, which is typically taken to be 5 at TCV, based on comparison between divertor power load measurements from LPs and IR thermography [64].

Immediately following the L–H transition, both the power and particle fluxes fall transiently, due to an increase in stored energy. Following this phase, it is found that increasing fuelling can reduce the power loads by ∼30%, although there does not appear to be a significant reduction in either total or peak ion flux.

The effect of a combination of fuelling and seeding was studied in similar plasmas as those in the fuelling scan, as illustrated in figure 14. In these shots, fuelling into the SOL at

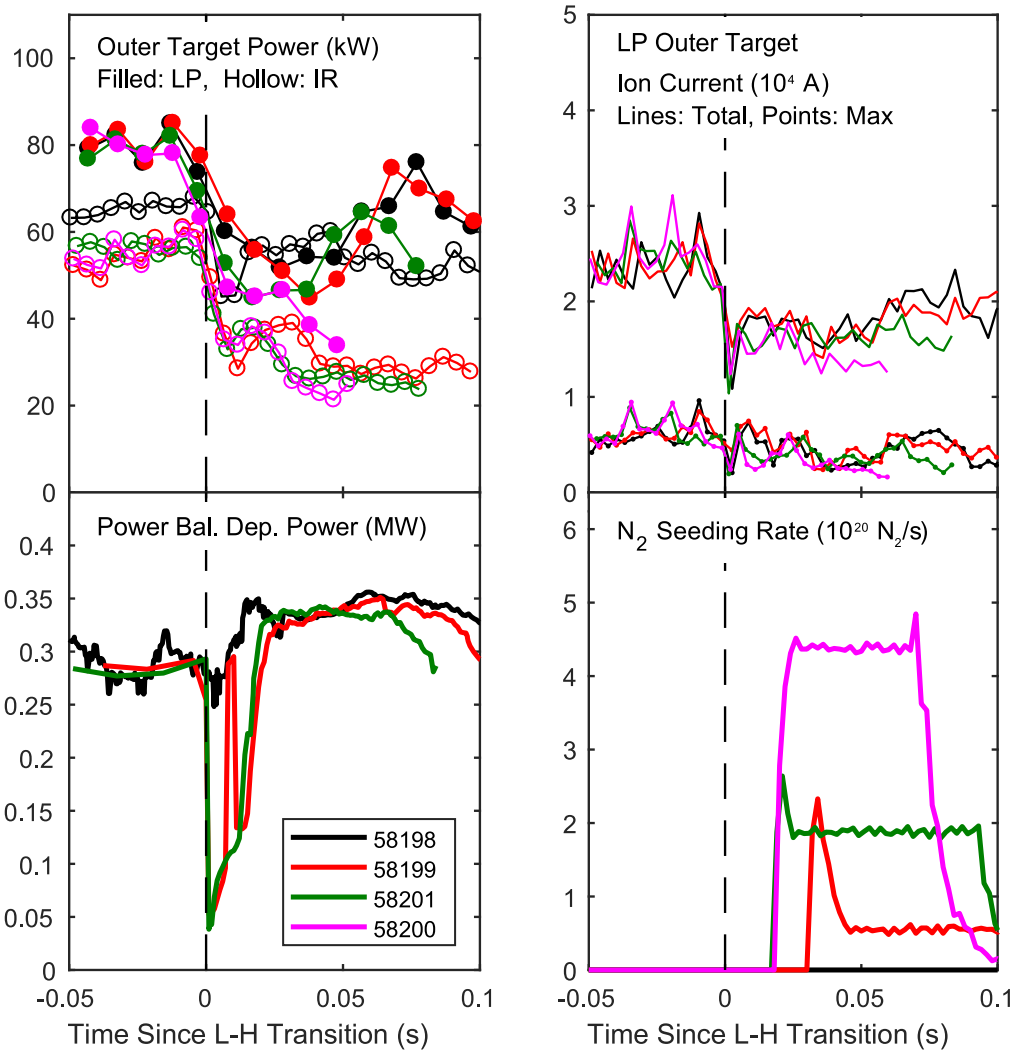

Figure 14. Evolution of the outer divertor power and particle loads with a combination of fuelling and increasing nitrogen seeding. The quantities plotted are the same as in the previous figure.

a rate of 9×10^{20} D_2/s was used in conjunction with nitrogen injected into the private flux region. The timing of the L–H transition was not perfectly reproducible, so the timing of the fuelling and seeding waveforms differ between shots. The total divertor power load is reduced by ~50% in the case with the highest level of seeding, compared with the shot with no seeding. There is also evidence of a modest reduction in the total ion flux, which is mostly due to a reduction in the peak of the profile. This would indicate that the divertor is in a state of partial detachment in terms of the power flux reaching the divertor, but less so in terms of the particle flux. This would indicate that nitrogen seeding is more effective than fuelling in mitigating the divertor particle and heat flux. A comparison of these results with scalings of the proximity to detachment with machine operating parameters (e.g. [65, 66]) is not currently possible, as the pressure gauge measurements do not have a sufficiently short time response to characterise the ELM-free phase.

4.2.4. Impurity line emission. In previous L-mode detachment studies on TCV (and on other devices, as discussed in section 2), the movement of the impurity emission front from the target to the X-point on the approach to detachment has been used to infer the cooling of the divertor leg and the proximity to the onset of detachment. For example, in figure 2 the emission front moves mid-way from the target to the X-point when the total ion flux to the outer divertor starts to roll over. This approach is applied here to estimate the efficacy of fuelling and seeding to cool the outer divertor leg in the shots presented in this section. The time evolution of the position of the impurity emission front is shown in figure 15, plotted as a function of time since the L–H transition. It is observed that the application of fuelling alone is sufficient for the emission front to move from the target to half way up the leg (see red curve in figure 15), close to the position where a roll over in the divertor ion flux occurs in L-mode experiments. However, further increasing the gas fuelling rate accelerates the core density ramp, causing the disruption to occur earlier, and so the impurity emission front does not advance further toward the X-point (this is evident in a separate fuelling scan conducted in shots 58 196, 58 192, 58 193, not shown). The application of increasing levels of seeding results in the emission front moving closer to the

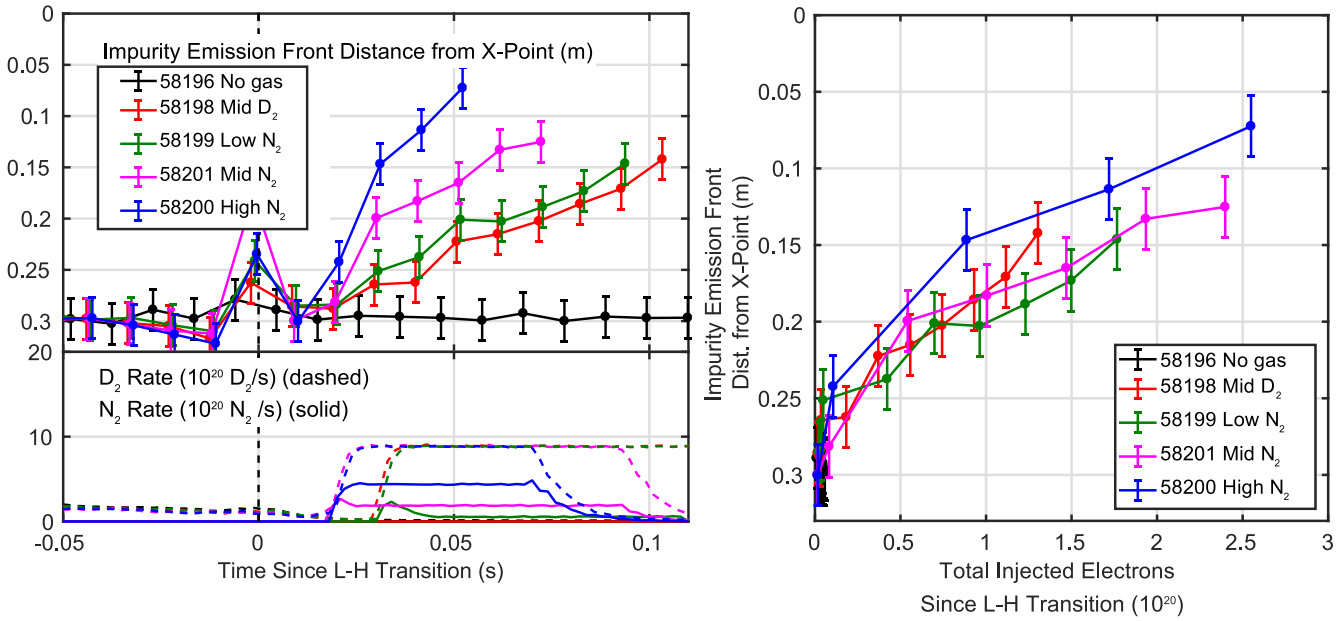

Figure 15. Movement of the impurity emission front along the outer leg in shots with fuelling and increasing nitrogen seeding in time (left) and number of injected electrons since the L–H transition (right).

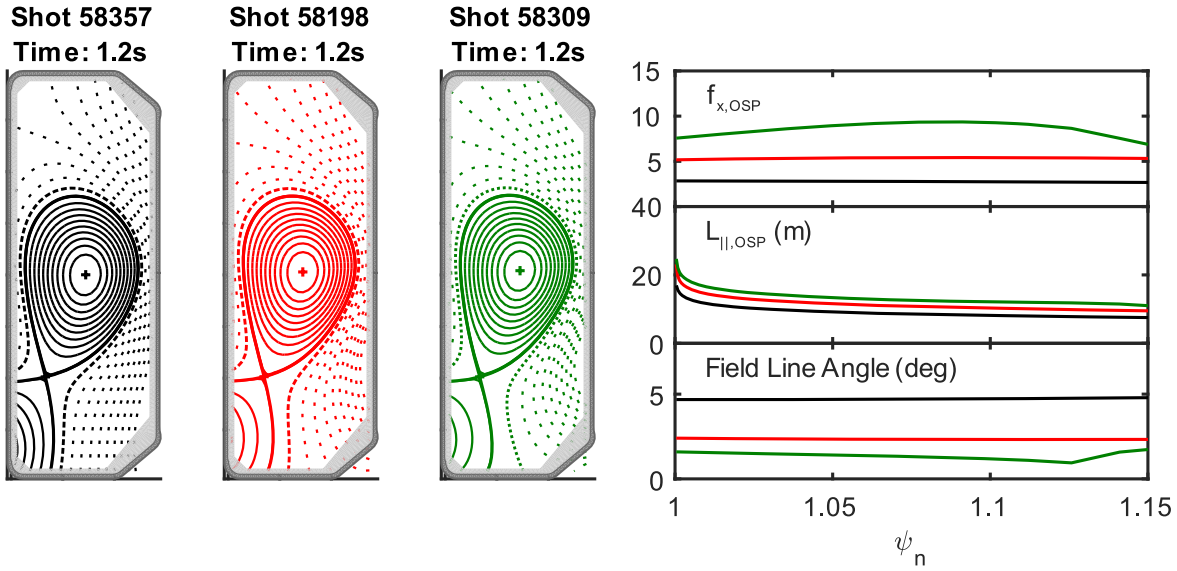

Figure 16. (Left) Equilibria of the shots in the poloidal flux expansion scan, (right) from top to bottom, radial profiles of poloidal flux expansion from the outer mid-plane to the outer divertor $f_{x,\mathrm{OSP}}$, field line connection length from the outer mid-plane to the outer divertor, $L_{||}$, and field line incidence angle to the divertor. The $\psi_n = 1.1$ surface is indicated by a thick dashed contour. The change is $f_{x,\mathrm{OSP}}$ and field line angle in shot 58 309 at $\psi_n = 1.13$ is due to an intersection with the sloping divertor tiles beyond $R = 0.965$ m.

X-point, and more quickly (green, magenta, and blue curves in figure 15). On this basis, it appears that nitrogen seeding is more efficient at cooling the divertor than fuelling. If the front location in these shots is compared with respect to the number of electrons injected during the H-mode phase, it is found that both fuelling and seeding have a similar effect. However, this is based on the assumption that the nitrogen is fully ionised in the divertor; if T_e in the divertor is assumed to be ~20 eV or less (e.g. see figure 24 for T_e and n_e profile measurements at the outer divertor target), the nitrogen ions are more likely to be lower charge states ($\sim N^{4+}$ assuming coronal equilibrium, lower if transport effects are significant), which would increase the slope of the nitrogen seeded front movement curves by >40%. The role of carbon sputtered from the divertor, particularly in the unseeded shots where carbon is likely a significant source of radiation, is currently unclear due to the lack of measurements of the carbon concentration and will be studied in future experiments with dedicated spectrometer measurements.

4.3. Influence of outer divertor poloidal flux expansion

In previous L-mode experiments using fuelling to reach divertor detachment [23, 39], the poloidal flux expansion

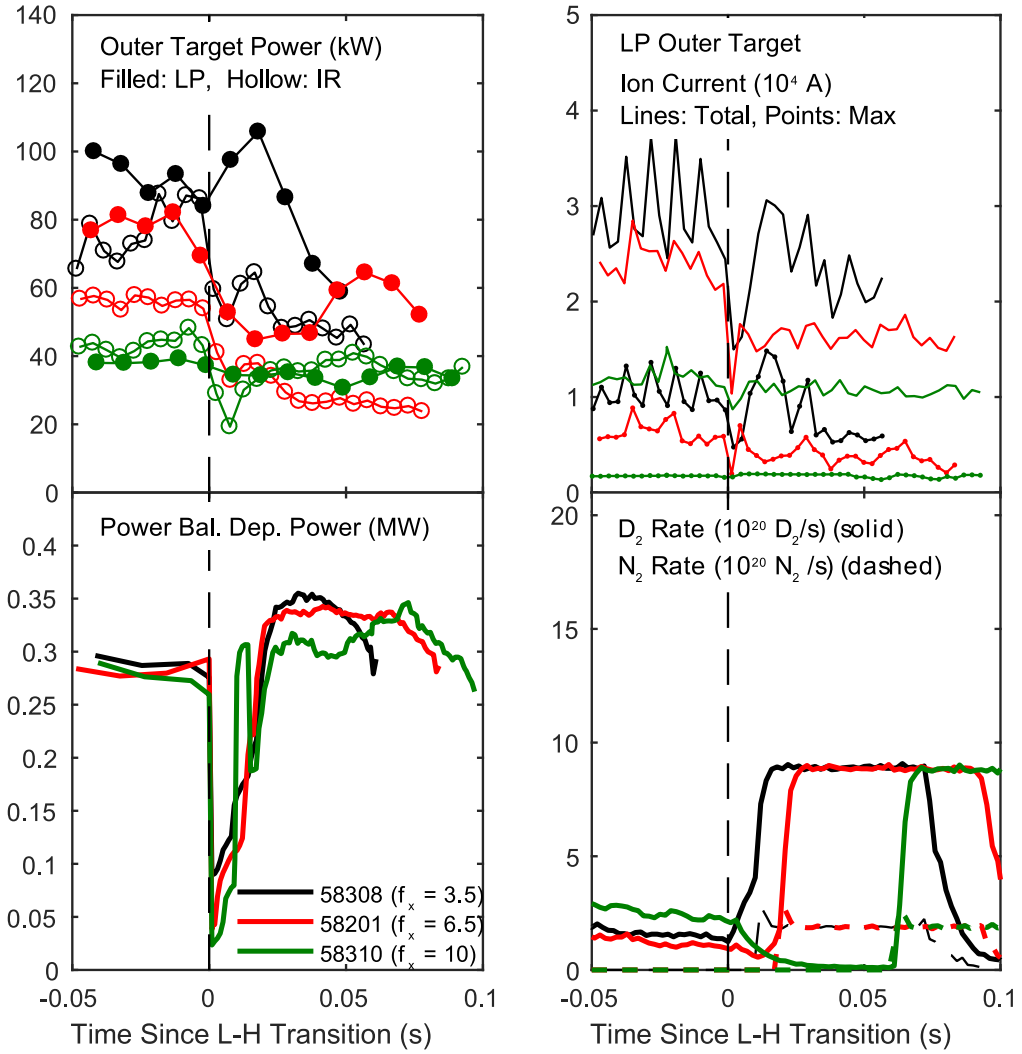

Figure 17. Evolution of the outer divertor power and particle loads in shots with different poloidal flux expansion at the outer divertor. The quantities plotted have the same meaning as in figures 13 and 14. The increased divertor power load in shot 58 201 detected by the Langmuir probes ∼40 ms after the L–H transition is thought to be an artefact in the analysed data.

from the outer mid-plane to the outer divertor was found to influence the highest achievable reduction in the divertor ion flux whilst the detachment threshold was not strongly affected. In the present H-mode experiments, fuelling and seeding are applied to shots with $f_{x,\mathrm{OSP}} = 3.5$, 6.5 and 10. Representative equilibria are shown in figure 16. The total outer divertor power load decrease with increasing $f_{x,\mathrm{OSP}}$ in accordance with the reduced field line incidence angle to the divertor target, as shown in figure 17. The total particle load and the peak value perpendicular to the target also decrease with increasing $f_{x,\mathrm{OSP}}$. This is thought to be due changes in the power and particle flux distribution between the inner and outer divertors, as observed in [17]. Comparison of the impurity emission front movement with fuelling and seeding (data from the fuelling scan are shown in figure 18) did not indicate that $f_{x,\mathrm{OSP}}$ strongly influences the cooling of the divertor leg, suggesting the redistribution of power between the inner and outer divertors is not sufficiently strong to play a role.

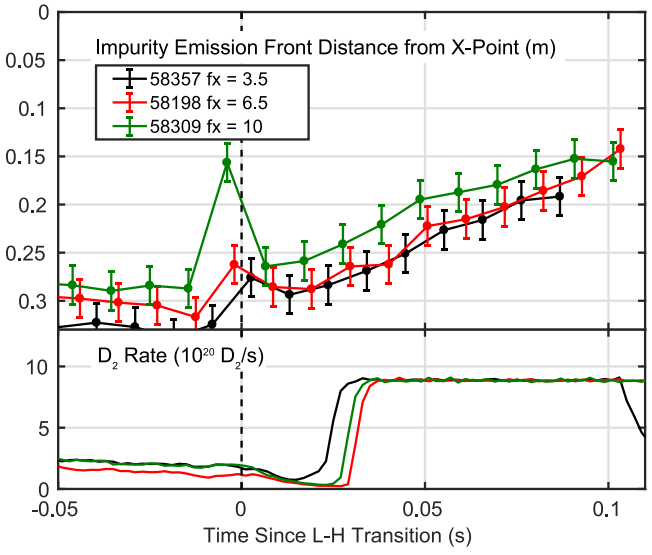

Figure 18. Evolution of the impurity emission front location in fuelled ELM-free H-mode shots with different outer divertor poloidal flux expansion.

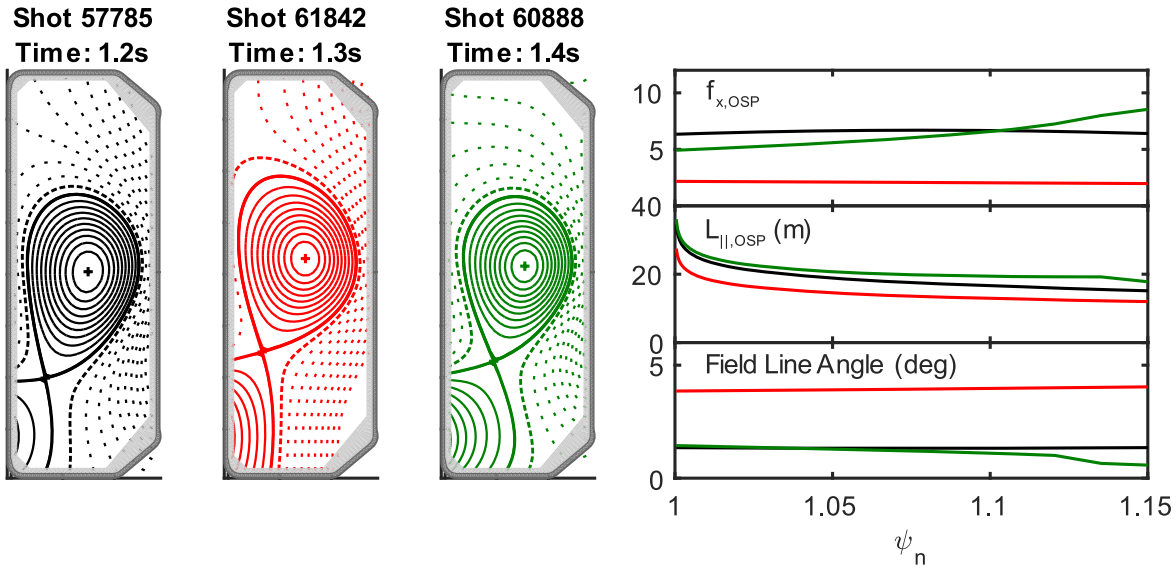

Figure 19. Representative equilibria of the 210 kA (left), 170 kA (centre) and 140 kA (right) ELMy H-mode scenarios, plotting the same properties as in figure 16.

5. ELMy H-mode experiments

5.1. General observations

Unlike the ELM-free experiments discussed previously, ELMy H-modes are normally quasi-stationary, with ELMs providing sufficient particle transport to regulate the particle content of the core. In these experiments, nitrogen seeding was used to promote cooling of the outer leg, and thereby approach detachment, in 3 scenarios of different plasma current—210, 170 and 140 kA, with equilibria shown in figure 19. From the consideration of the pedestal temperature and density discussed in section 3.2, the higher pedestal temperature and lower density would indicate these scenarios are more challenging to detach than the ELM-free shots.

The time evolution of a 210 kA discharge with strong nitrogen seeding into the private flux region is shown in figure 20. The plasma enters a phase with regularly spaced ELMs at 0.95 s, shortly before the introduction of nitrogen seeding at 1.01 s. The seeding results in a factor ∼2 increase in the total radiation, a steady reduction of the ELM amplitude and a ∼30% reduction in the energy confinement time relative to the IPB98(y,2) scaling (although the stored energy is constant), and eventually a back-transition to L-mode.

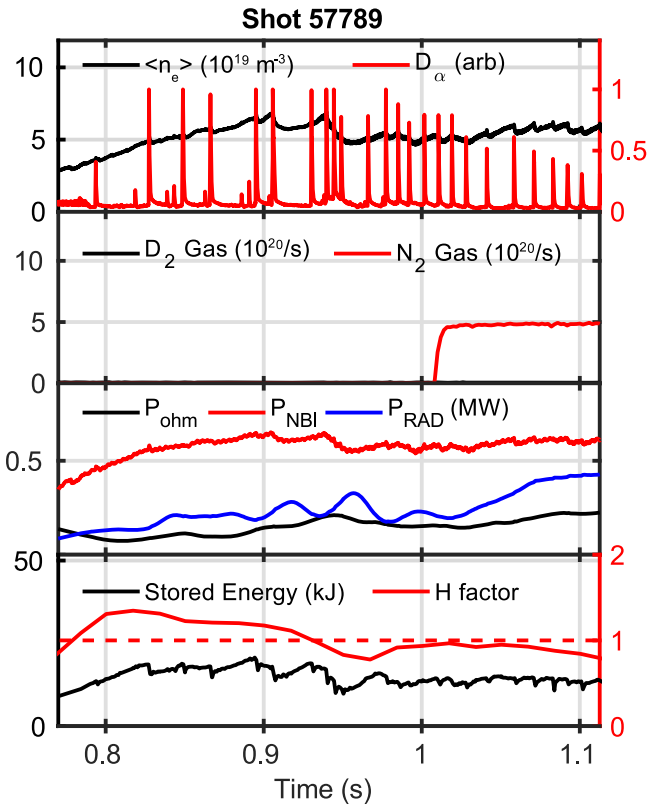

Figure 20. Overview of a nitrogen seeded ELMy H-mode shot, showing (from top to bottom) the evolution of the line average density, divertor D_α emission, gas fuelling and seeding rates, plasma power sources and sinks, stored energy and confinement quality.

5.2. Global power balance

The terms in the global power balance in these ELMy H-mode plasmas are similar to those considered in the ELM-free cases discussed in the previous section, except that the average power transported through the SOL by ELMs should also be accounted for. The ELM losses are estimated using the difference between measurements of the stored energy from a diamagnetic loop before and after an ELM and after any over-shoot of the measurement. A time average of the ELM energy loss is estimated by performing a linear fit to the product of the energy loss per ELM and the ELM frequency over the ELMing phase. The radiation losses between ELMs are estimated by filtering the bolometer data (that are filtered with a ∼350 Hz Bessel filter to remove the effects of noise) with a 10 ms wide moving window that returns the minimum

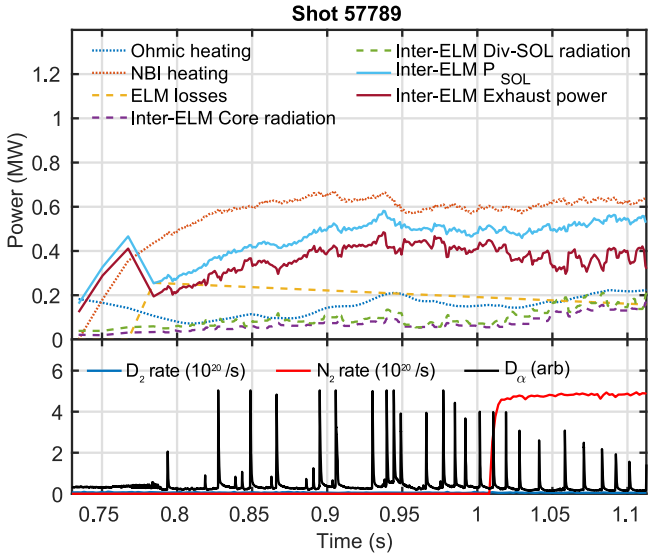

Figure 21. Global power balance in a nitrogen ELMy H-mode shot. The quantities plotted have the same meaning as in figure 8, except the rate of change of stored energy ($\mathrm{d}W/\mathrm{d}t$) is replaced with the change in stored energy due to ELMs.

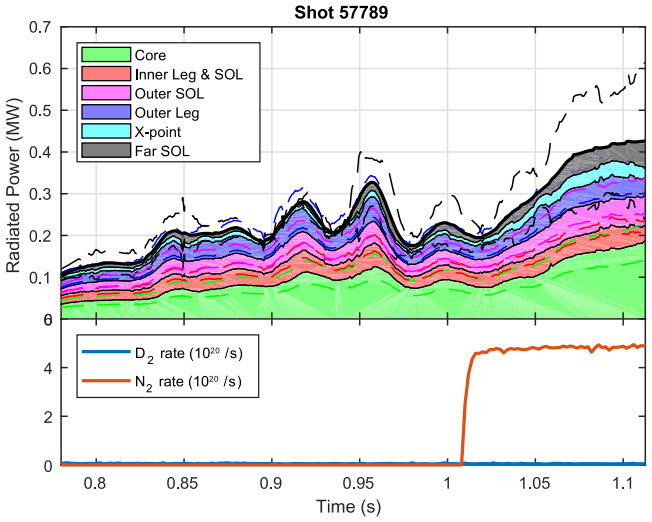

Figure 22. Breakdown of the inter-ELM radiated power measured by the foil bolometers in terms of its origin within the plasma for a nitrogen seeded ELMy H-mode shot. The dashed lines indicate uncertainties in each measurement.

value within the window. This method robustly removes the radiation due to ELMs but cannot resolve changes in the radiated power between each ELM.

The global power balance of an ELMy H-mode shot with strong nitrogen seeding is shown in figure 21. The application of seeding leads to an increase in radiation both inside and outside the confined plasma in equal measure, however P_{SOL} is maintained at ~700 kW as the increase in core radiation is compensated by an increase in the ohmic heating power (possibly due to an increase in the impurity content of the core, Z_{eff}, but ELM-resolved measurements are not available to verify this). The estimated power deposited on plasma-facing surfaces, referred to as the inter-ELM exhaust power in figure 21, is reduced from ~600 kW to 500–550 kW due to the increased radiation in the divertor and SOL as a consequence of the nitrogen injection. During the nitrogen seeding phase, the ELM amplitude diminishes until the H-mode period ends with a back-transition to L-mode.

The distribution of radiative losses in this shot is shown in figure 22, with broadly similar characteristics as the ELM-free shots. Nitrogen seeding leads to strong increase in the radiation losses in the core, far SOL and X-point, compared with only modest changes in the radiation from the inner and outer divertor legs.

5.3. Pedestal profile evolution

In the shot discussed in the previous sections, strong nitrogen seeding resulted in the loss of H-mode. An examination of the pedestal density and temperature profiles before and after the seeded phase is shown in figure 23. This equilibrium is not optimised for measurements of the pedestal profiles, however it is possible to deduce trends in the pedestal top properties. There is a clear increase in the electron density profiles, with

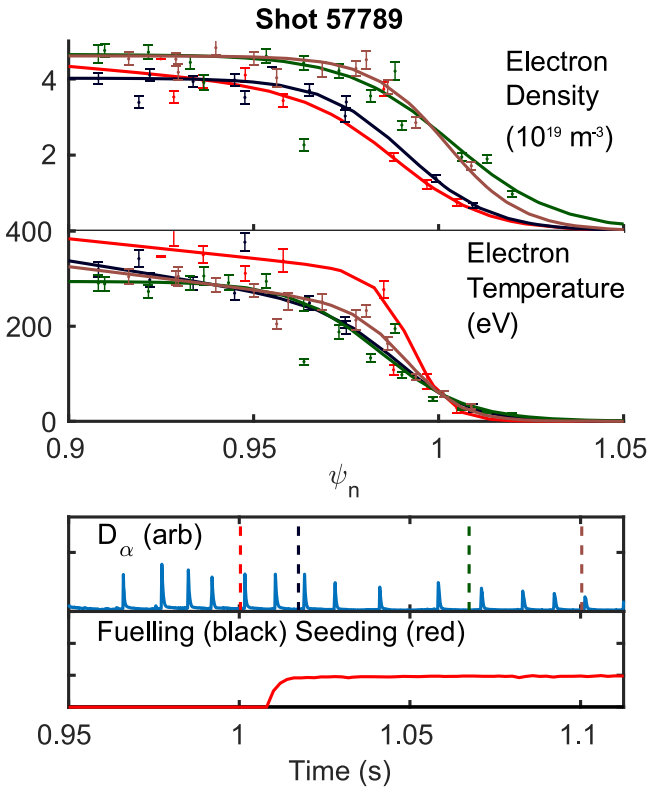

Figure 23. Evolution of pedestal temperature and density profiles during a nitrogen seeding ramp experiment.

the pedestal top density increasing from $\sim 3.7 \times 10^{19}$ to 4.5×10^{19} m^{-3} (22% increase). Conversely, the pedestal top temperature reduced from ~300 eV at the start of the seeding phase to ~240 eV (20% decrease) before the back-transition to L-mode. The countervailing trends in the temperature and density profiles result in the pressure profile being largely

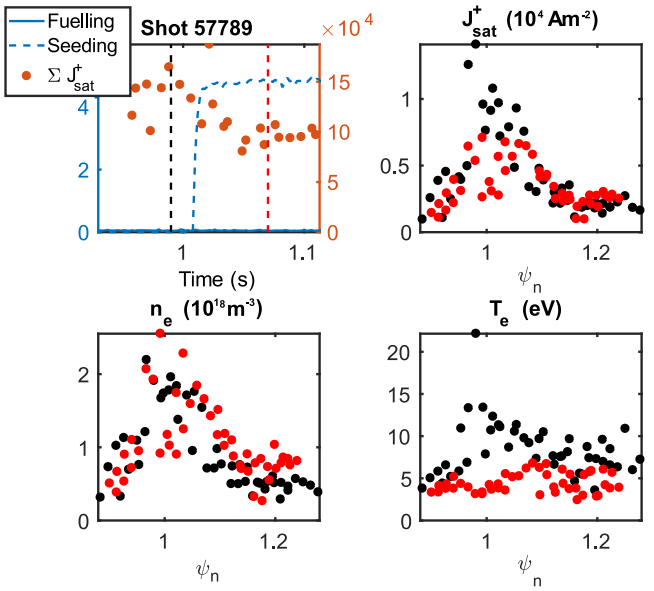

Figure 24. Summary of Langmuir probe measurements. (upper left) time traces of the nitrogen seeding rate and total ion flux to the outer divertor (upper right, lower left, lower right) Ion saturation current density, electron density and electron temperature profiles measured at the times indicated by dashed lines in the upper right plot.

unchanged. Similar trends are observed in the other ELMy scenarios studied, e.g. the 140 kA shots (not shown), which shows no trend in the pedestal top density and the temperature falls from ∼340 to ∼220 eV. The separatrix electron temperature is constrained to conform with estimates from the two-point model, which vary from 60 to 70 eV between scenarios. As P_{SOL} is approximately maintained during the seeding phase, the two-point model, including the measured radiation losses, predicts no change in the upstream temperature.

5.4. Outer divertor power and particle loads

The main effect of nitrogen injection into the ELMy H-mode plasmas considered here is to strongly reduce electron temperature profile across the outer divertor. This is illustrated in figure 24, which shows the time evolution of the total ion flux to the outer divertor and profiles of the ion saturation current, electron density and electron temperature before and after the application of nitrogen seeding.

Comparison of the target profiles before and after the application of seeding shows that the most pronounced effect is on the electron temperature profile. The initially peaked profile, with a maximum temperature of ∼20 eV flattens, and the peak temperature drops to ∼5 eV. Conversely, the electron density profiles are broadly similar, given the scatter in the data, after the seeding is applied. The peak plasma pressure at the outer target is reduced by a factor ∼5, whereas the upstream temperature is broadly unchanged, indicating the plasma in the vicinity of the separatrix is partially detached [67]. The reduction in the electron temperature profile leads to a factor ∼2 reduction in the total power deposited to the outer divertor.

5.5. Influence of outer divertor target major radius

In previous L-mode experiments using fuelling to detach the outer divertor [23] it was found that varying the major radius of the outer strike point did not significantly affect the detachment characteristics. This is contrary to predictions from a modified two-point model [68] that predict the electron temperature and density at the target vary with the ratio of the upstream and target major radii R_u, R_t respectively, according to $T_e \propto \left(\frac{R_u^2}{R_t^2}\right)$ and $n_e \propto \left(\frac{R_t^2}{R_u^2}\right)$. To ascertain whether this behaviour is evident in ELMy H-mode experiments, shots were carried out with the strike point major radius R_{T} placed at 0.75 and 1.03 m and $I_{\mathrm{p}} = 170$ kA ($q_{95} = 4.1$), 1 MW of NBI heating and similar Greenwald fraction (f_{G} ($R_{\mathrm{T}} = 0.75$ m) ∼ 0.37, f_{G} ($R_{\mathrm{T}} = 1.03$ m) ∼ 0.42) and poloidal flux expansion at the outer divertor ($f_{x,\mathrm{OSP}}$ ($R_{\mathrm{T}} = 0.75$ m) ∼ 2.4, $f_{x,\mathrm{OSP}}$ ($R_{\mathrm{T}} = 1.03$ m) = 2.2), as shown in figure 25. Nitrogen seeding into the private flux region was used to cool the divertor to promote detachment of the outer divertor.

Our primary measure of the progress toward detachment is the location of the impurity emission front. The time evolution of the front location in these cases is shown in figure 26. The emission front moves from the target toward the X-point following the start of the nitrogen injection. These data have been filtered to show measurements between and during ELMs, as ELMs move the emission front to the divertor surface irrespective of the location of the front between ELMs, consistent with the ELMs 'burning through' the cooling divertor leg.

Between ELMs, the difference in the impurity front movement between the smaller and larger R_{T} cases is rather subtle, which was also observed in L-mode experiments. It cannot be ruled out that this change could be due to the small differences in the parallel connection length or poloidal leg length, and will be addressed in future modelling studies. The impurity emission front starts to move away from the target at the same time in both cases, although the speed of the front movement appears to be slower in the larger R_{T} case, taking 25 ms to move from the target to ∼10 cm from the X-point in the larger R_{T} experiment, compared with 19.5 ms at lower R_{T}. It is possible that the slower motion of the front location in the larger R_{T} case is due in part to the higher ELM frequency (∼100 Hz compared with ∼92 Hz in the lower R_{T} case), however the data suggest that the front location after an ELM can return to its pre-ELM position in the time between frames, 2.5 ms, so this effect alone is unlikely to explain this behaviour. Direct comparison of the target electron density and temperature profiles in the large RT scenario is not currently possible as the probe array does not extend beyond $R = 0.965$ m. However, additional probe arrays will be installed in an upcoming upgrade [59] that will also allow for studies in a more closed divertor.

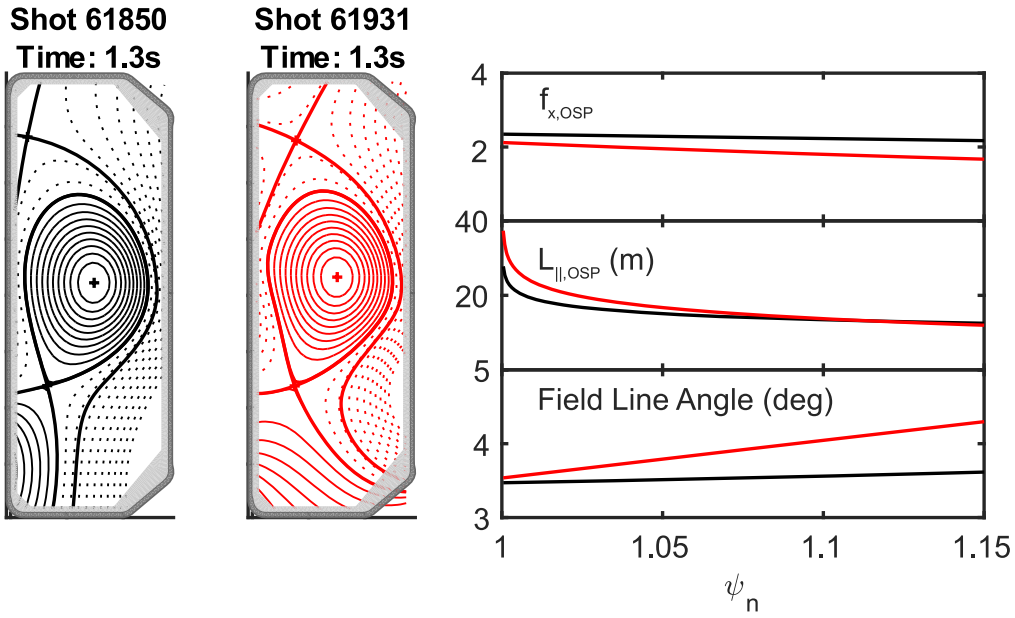

Figure 25. Equilibria from experiments to study the effect of varying the total flux expansion out the outer divertor by varying the major radius from 0.75 to 1.03 m.

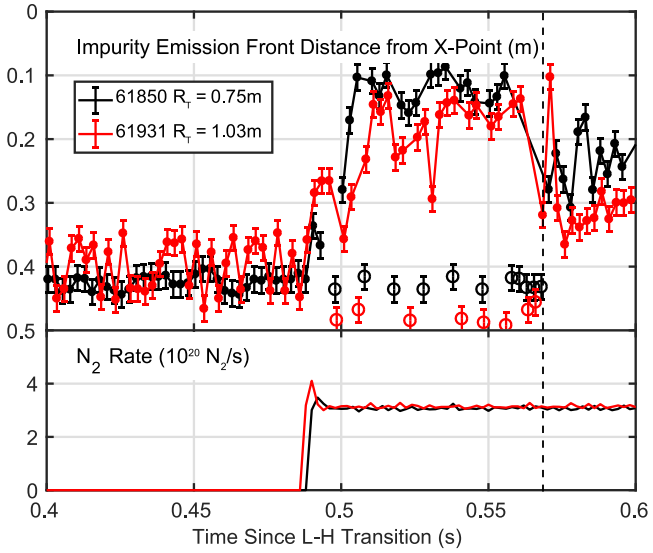

Figure 26. Outer leg impurity front location between ELMs in shots with different strike point major radius. Measurements taken during ELMs are shown as hollow points. A back-transition to L-mode ~0.057 s after the L–H transition is indicated by a dashed line.

6. Summary and conclusions

Access to partial detachment in ELM-free and ELMy H-mode TCV discharges, where there is a noticeable reduction in the outer divertor power load, has been explored using fuelling and nitrogen injection from the divertor in a range of divertor configurations. A characterisation of the H-mode operating space has been carried out, in terms of assessing the conditions required to enter and sustain H-mode. It has been observed that the heating power required to cross the L–H transition threshold, where the density is close to the minimum in the $P_{\mathrm{L-H}}/n_{\mathrm{e}}$ curve, is relatively insensitive to the outer target poloidal flux expansion or major radius in the single null configuration, nor is there a large difference in threshold power between these variants on the single null and the snowflake minus configurations studied.

The limits to quasi-stationary H-mode operation have been quantified, including transitions from ELMy to ELM-free conditions and the disruptive limits in ELM-free plasmas and back-transition to L-mode in ELMy scenarios. ELM-free H-mode scenarios have some positive properties to aid progress toward divertor detachment, including moderate separatrix electron temperature (~40–50 eV) and relatively high separatrix density ($>2.5 \times 10^{19}$ m^{-3}). However, the ELM-free phase typically have a duration of <200 ms, which decreases when fuelling or seeding is applied. Using a combination of fuelling and nitrogen seeding, a small reduction in the peak and total ion flux to the outer divertor was observed, and the total power deposited to the outer divertor was reduced by a factor ~2. A comparison of fuelling and seeding on divertor cooling, quantified in terms of movement of the impurity radiation front from the target toward the X-point was carried out, showing that seeding resulted in stronger cooling of the divertor, but the two gases have the same effect on the impurity front location in terms of the number of electrons injected (see figure 15). The effect of poloidal flux expansion on divertor cooling was studied in both fuelled and nitrogen seeded experiments, which was not found to play a strong role.

Nitrogen seeding in ELMy H-mode plasmas was found to significantly reduce the electron temperature at the outer divertor, reducing the peak temperature by a factor of ~3–4, while the electron density profile was broadly similar, and slightly elevated near the peak of the profile, indicating that the outer divertor is in a state of partial detachment. A factor ~2 reduction in the total power load to the outer divertor between ELMs was observed. The effect of the outer target

major radius on the movement of the impurity radiation was explored in experiments with the strike point at $R = 0.75$ and 1.03 m. The movement of the impurity radiation front from the target toward the X-point was found to be ~20% slower when the strike point was moved to larger radius, which could suggest that the front is less sensitive to changes in the divertor conditions. Nitrogen seeding results in a steady reduction in the ELM amplitude and a back-transition to L-mode. The duration of the ELMy H-mode phase was found to be independent of the major radius of the strike point.

Analysis of both the ELMy and ELM-free shots indicate that strong fuelling and seeding result in the loss of H-mode and shorter H-mode phases respectively, which suggests that the main impediment to making further progress towards achieving greater divertor heat and particle flux mitigation is set by the requirement to remain in H-mode and preferably in an ELMy, quasi-stationary state. Further progress looks likely when the new baffle structures are installed in TCV [27, 59] that will promote radiative losses by increasing divertor neutral compression and elevating the divertor electron density (as the radiated power from a given species is proportional to n_e^2 at fixed concentration this could be an important effect) and increased neutral beam heating may elevate the pedestal top density before a transition from ELMy to ELM-free H-mode occurs.

This work provides a basis for future detachment studies in H-mode on TCV, including extending this work to include other alternative divertor concepts such as the double null, snowflake and X-point target at higher heating power and to continue explore the role of the divertor configuration in mediating ELM heat and particle fluxes. The excellent diagnostics capabilities can be further leveraged to characterise the plasma conditions in attached and detached conditions to allow for detailed modelling studies to facilitate greater understanding.

Acknowledgments

This work has been carried out within the framework of the EUROfusion Consortium and has received funding from the Euratom research and training programme 2014–2018 under Grant Agreement No. 633053 and from the RCUK Energy Programme [Grant No. EP/P012450/1]. The views and opinions expressed herein do not necessarily reflect those of the European Commission. This work was supported in part by the Swiss National Science Foundation.

ORCID iDs

J R Harrison https://orcid.org/0000-0003-2906-5097
C Theiler https://orcid.org/0000-0003-3926-1374
O Février https://orcid.org/0000-0002-9290-7413
R Maurizio https://orcid.org/0000-0001-9896-6732
K Verhaegh https://orcid.org/0000-0002-0500-2764
B Lipschultz https://orcid.org/0000-0001-5968-3684
S Henderson https://orcid.org/0000-0002-8886-1256
B Labit https://orcid.org/0000-0002-0751-8182
H Reimerdes https://orcid.org/0000-0002-9726-1519
U Sheikh https://orcid.org/0000-0001-6207-2489
C K Tsui https://orcid.org/0000-0002-7346-8312

References

[1] Shimada M *et al* 2007 *Nucl. Fusion* **47** S1–17
[2] Wenninger R P *et al* 2014 *Nucl. Fusion* **54** 114003
[3] Zohm H *et al* 2013 *Nucl. Fusion* **53** 073019
[4] Pitts R A *et al* 2017 *Nucl. Mater. Energy* **12** 60–74
[5] Takase H 2001 *J. Phys. Soc. Japan* **70** 609
[6] Kotschenreuther M, Valanju P M, Mahajan S M and Wiley J C 2007 *Phys. Plasmas* **14** 072502
[7] Ryutov D D 2007 *Phys. Plasmas* **14** 064502
[8] Valanju P M, Kotschenreuther M, Mahajan S M and Canik J 2009 *Phys. Plasmas* **16** 056110
[9] LaBombard B *et al* 2015 *Nucl. Fusion* **55** 053020
[10] Takizuka T, Tokunaga S, Hoshino K, Shimizu K and Asakura N 2015 *J. Nucl. Mater.* **463** 1229
[11] Covele B *et al* 2017 *Nucl. Fusion* **57** 086017
[12] Havlíčková E *et al* 2014 *Plasma Phys. Control. Fusion* **56** 075008
[13] Moulton D *et al* 2017 *Plasma Phys. Control. Fusion* **59** 065011
[14] Ryutov D D, Cohen R H, Farmer W A, Rognlien T D and Umansky M V 2014 *Phys. Scr.* **89** 088002
[15] Vijvers W A J, Canal G P, Labit B, Reimerdes H, Tal B, Coda S, De Temmerman G C, Duval B P, Morgan T W and Zielinski J J 2014 *Nucl. Fusion* **54** 023009
[16] Walkden N R, Labit B, Reimerdes H, Harrison J, Farley T, Innocente P and Militello F 2018 Fluctuation characteristics of the TCV snowflake divertor measured with high speed visible imaging *Plasma Phys. Control Fusion* **60** 115008
[17] Maurizio R, Elmore S, Fedorczak N, Gallo A, Reimerdes H, Labit B, Theiler C, Tsui C K and Vijvers W A J 2018 *Nucl. Fusion* **58** 016052
[18] Gallo A *et al* 2018 *Plasma Phys. Control. Fusion* **60** 014007
[19] Pitts R A *et al* 2001 *J. Nucl. Mater.* **290–293** 940–6
[20] Pitts R A, Refke A, Duval B P, Furno I, Joye B, Lister J B, Martin Y, Moret J-M, Romers R and Weisen H 1999 *J. Nucl. Mater.* **266–269** 649–53
[21] Harrison J R *et al* 2017 *Nucl. Mater. Energy* **12** 1071–6
[22] Verhaegh K *et al* 2017 *Nucl. Mater. Energy* **12** 1112–7
[23] Theiler C, Lipschultz B, Harrison J, Labit B, Reimerdes H, Tsui C, Vijvers W A J, Boedo J A and Duval B P 2017 *Nucl. Fusion* **57** 072008
[24] Labit B *et al* 2017 *Nucl. Mater. Energy* **12** 1015–9
[25] Reimerdes H *et al* 2013 *Plasma Phys. Control. Fusion* **55** 124027
[26] Coda S *et al* 2017 *Nucl. Fusion* **57** 102011
[27] Fasoli A and Team T C V 2015 *Nucl. Fusion* **55** 043006
[28] Hofmann F *et al* 1994 *Plasma Phys. Control. Fusion* **36** B277
[29] Karpushov A *et al* 2017 *Fusion Eng. Des.* **123** 468–72
[30] Pitts R A, Alberti S, Blanchard P, Horacek J, Reimerdes H and Stangeby P C 2003 *Nucl. Fusion* **43** 1145–66
[31] Février O, Theiler C, De Oliveira H, Labit B, Fedorczak N and Baillod A 2018 *Rev. Sci. Instrum.* **89** 053502
[32] Veres G, Pitts R A, Wischmeier M, Gulejova B, Horacek J and Kálvin S 2007 *J. Nucl. Mater.* **363–365** 1104–9
[33] Linehan B *et al* 2018 *Rev. Sci. Instrum.* **89** 103503
[34] Vijvers W A J, Mumgaard R T, Andrebe Y, Classen I G J, Duval B P and Lipschultz JINST B 2017 **12** C12058
[35] Fenstermacher M E *et al* 1997 *Phys. Plasmas* **4** 1761

[36] Boswell C J and Terry J L 2002 *IEEE Trans. Plasma Sci.* **30** 78
[37] Huber A *et al* 2012 *Rev. Sci. Instrum.* **83** 10D511
[38] Harhausen J *et al* 2007 *Proc. 34th EPS Conf.*
[39] Reimerdes H *et al* 2017 *Nucl. Fusion* **57** 126007
[40] Hawke J *et al J. Instrum.* **12** C12005
[41] Groth M *et al* 2011 *J. Nucl. Mater.* **415** S530–4
[42] Christen N *et al* 2017 *Plasma Phys. Control. Fusion* **59** 105004
[43] Maggi C F *et al* 2014 *Nucl. Fusion* **54** 023007
[44] Battaglia D *et al* 2013 *Nucl. Fusion* **53** 113032
[45] Gohil P *et al* 2011 *Nucl. Fusion* **51** 103020
[46] Ryter F *et al* 2014 *Nucl. Fusion* **54** 083003
[47] Liu Z X *et al* 2013 *Nucl. Fusion* **53** 073041
[48] Hubbard A E *et al* 2007 *Phys. Plasmas* **14** 056109
[49] Meyer H *et al* 2011 *Nucl. Fusion* **51** 113011
[50] Scaggion A, Martin Y and Reimerdes H 2012 *P2.093, Proc. 39th EPS Conf.*
[51] Karpushov A *et al* 2011 *Fusion Eng. Des.* **86** 868–71
[52] Pereverzev G V and Yushmanov P N 2002 ASTRA, Automated System for Transport Analysis in a Tokamak *IPP Report* 5/98 Max-Planck-Institut für Plasmaphysik, Garching
[53] Karpushov A N *et al* 2015 *Fusion Eng. Des.* **96–97** 493–7
[54] Martin Y R *et al* 2008 *J. Phys.: Conf. Ser.* **123** 012033
[55] Piras F, Coda S, Duval B P, Labit B, Marki J, Yu Medvedev S, Moret J-M, Pitzschke A and Sauter O 2010 *Phys. Rev. Lett.* **105** 155003
[56] Groebner R J and Carlstrom T N 1998 *Plasma Phys. Control. Fusion* **40** 673
[57] Greenwald M 2002 *Plasma Phys. Control. Fusion* **44** R27
[58] Harrison M F A and Hotston E S 1990 *J. Nucl. Med.* **176–7** 256
[59] Reimerdes H *et al* 2017 *Nucl. Mater. Energy* **12** 1106–11
[60] Eich T *et al* 2013 *Nucl. Fusion* **53** 093031
[61] ITER Physics 1999 Expert groups on confinement and transport and confinement modelling and database *Nucl. Fusion* ITER physics basis editors **39** 2175
[62] Stangeby P C 2000 *The Plasma Boundary of Magnetic Fusion Devices* (Bristol: IOP Publishing)
[63] Moret J-M, Duval B P, Le H B, Coda S, Felici F and Reimerdes H 2015 *Fusion Eng. Des.* **91** 1–15
[64] Marki J *et al* 2007 *J. Nucl. Mater.* **363** 382
[65] Kallenbach A *et al* 2015 *Nucl. Fusion* **55** 053026
[66] Kallenbach A, Bernert M, Dux R, Reimold F and Wischmeier M 2016 *Plasma Phys. Control. Fusion* **58** 045013
[67] Loarte A *et al* 1998 *Nucl. Fusion* **38** 331
[68] Petrie T W 2013 *Nucl. Fusion* **53** 113024